Deglacial ice sheet instabilities induced by proglacial lakes

Aurelien Quiquet[1], Christophe dumas[2], Didier Paillard[3], Gilles Ramstein[4], Catherine Ritz[5], and Didier M. Roche[6]

[1]Universite Paris-Saclay
[2]CEA
[3]Laboratoire des Sciences du Climat et de l'Environnement/IPSL - CEA/CNRS/UVSQ
[4]Laboratoire des Sciences du Climat et de l'Environnement
[5]Université Grenoble Alpes
[6]LSCE

November 21, 2022

Abstract

During the last deglaciation (21 - 7 kaBP), the gradual retreat of Northern Hemisphere ice sheet margins produced large proglacial lakes. While the climatic impacts of these lakes have been widely acknowledged, their role on ice sheet grounding line dynamics has received very little attention so far. Here, we show that proglacial lakes had dramatic implications for the North American ice sheet dynamics through a self-sustained mechanical instability which has similarities with the known marine ice sheet instability albeit providing fast retreat of large portions of the ice sheet over the continent. Systematically reproduced in the latest stage of the deglaciation, this mechanism could provide a physical origin for the debated melt water pulse 1B. Echoing our knowledge of Antarctic ice sheet dynamics, they are another manifestation of the importance of grounding line dynamics for ice sheet evolution.

Deglacial ice sheet instabilities induced by proglacial lakes

Aurélien, Quiquet[1], Christophe, Dumas[1], Didier, Paillard[1],Gilles, Ramstein[1], Catherine, Ritz[2], Didier M., Roche[1,3]

[1]Laboratoire des Sciences du Climat et de l'Environnement, LSCE/IPSL, CEA-CNRS-UVSQ, Université Paris-Saclay, F-91191 Gif-sur-Yvette, France
[2]Université Grenoble Alpes, CNRS, IRD, Grenoble INP, IGE, 38000 Grenoble, France
[3]Vrije Universiteit Amsterdam, Faculty of Science, Cluster Earth and Climate, de Boelelaan 1085, 1081HV Amsterdam, The Netherlands

Key Points:

- The North American proglacial lakes induce an ice sheet instability during the last deglaciation
- This mechanical instability could explain half of the mass loss for the final stage of the North American ice sheet
- This mechanism could provide a physical origin for the debated melt water pulse 1B

Corresponding author: Aurélien Quiquet, `aurelien.quiquet@lsce.ipsl.fr`

Abstract
During the last deglaciation (21 - 7 kaBP), the gradual retreat of Northern Hemisphere ice sheet margins produced large proglacial lakes. While the climatic impacts of these lakes have been widely acknowledged, their role on ice sheet grounding line dynamics has received very little attention so far. Here, we show that proglacial lakes had dramatic implications for the North American ice sheet dynamics through a self-sustained mechanical instability which has similarities with the known marine ice sheet instability albeit providing fast retreat of large portions of the ice sheet over the continent. Systematically reproduced in the latest stage of the deglaciation, this mechanism could provide a physical origin for the debated melt water pulse 1B. Echoing our knowledge of Antarctic ice sheet dynamics, they are another manifestation of the importance of grounding line dynamics for ice sheet evolution.

Plain Language Summary

While ice sheet contribution to future sea level rise remains uncertain, the last deglaciation provide an unique opportunity to understand the mechanisms behind large-scale ice sheet collapses. In recent years, ice sheet models have substantially improved as they now better represent ice dynamics than they used to. Here we use such a model to quantify for the first time the importance of proglacial lakes on ice sheet dynamics. We show that these lakes could be responsible for large-scale ice sheet collapses due to a flotation instability. The proglacial lake ice sheet instability could be an additional mechanism explaining observed late deglacial melt water pulses.

1 Introduction

Proglacial lakes have formed, evolved and drained in response to ice sheet changes throughout the Pleistocene (Teller, 1995). These lakes form at an ice margin by ice and/or moraine damming or in depressed basins. During the last deglaciation (21 - 7 kaBP), these lakes were a common feature of the Northern Hemisphere landscape, spanning a range of sizes reaching up several thousands of square kilometres in extent (Carrivick & Tweed, 2013). These lakes can be short-lived or last for several thousand years and may experience abrupt changes in water level (Teller & Leverington, 2004). These abrupt water level drops have sometimes resulted in large lake outbursts that probably had important consequences on the global climate owing to the large resulting freshwater flux to the oceans (Teller & Leverington, 2004). It is widely acknowledged, for example, that the abrupt drainage at 8.2 kaBP of Lake Agassiz-Ojibway, the largest known lake on Earth, which existed for thousands of years, induced a widespread cooling of the Northern Hemisphere via a slowdown of the Atlantic circulation (Barber et al., 1999; Wiersma & Renssen, 2006). Proglacial lakes have also had an impact at the regional scale, in particular for ice sheet surface mass balance, reducing summer ablation and favouring ice growth (Hostetler et al., 2000; Krinner et al., 2004). As the climatic importance of these lakes is well established, it is surprising perhaps that their role in ice sheet mechanics has received very little attention so far. Yet, using conceptual models for ice ages, some authors have hypothesised that these lakes could be responsible for Pleistocene ice volume oscillations, favouring calving and thus enhancing rapid ice retreat (Pollard, 1982; Fowler et al., 2013). This hypothesis has hitherto been tested with comprehensive physically-based numerical ice sheet models. Here, we use a set of numerical model experiments to study the impact of large proglacial lakes on ice sheet grounding line dynamics and to quantify their potential contribution to sea level rise accelerations during the last deglaciation.

Sea-level archives suggest that the deglacial rate of sea level rise has been far from linear, with episodic rapid accelerations (Lambeck et al., 2014). Amongst these events, the melt water pulse 1A (MWP-1A) is the most prominent feature with 14 to 18 metres of sea level rise in 340 years between 14.65 kaBP and 14.31 kaBP (Deschamps et al., 2012).

Later in the deglaciation, between 11.45 kaBP and 11.1 kaBP, another event, the melt water pulse 1B (MWP-1B), could also have been as large as about 14 metres over 350 years (Abdul et al., 2016) even if its existence is controversial due to its absence in some archives (Bard et al., 2016). These events suggest large-scale ice sheet collapses. So far, our understanding of the underlying processes leading to such ice sheet collapses is limited.

If there is no consensus on the geographic origin of the freshwater outbursts during these events (Liu et al., 2016) the comprehensive glacial histories of ICE-6G_C (Peltier et al., 2015) and GLAC-1D (Tarasov et al., 2012; Ivanovic et al., 2016), derived from inversion of indicators for modern surface subsidence measurements and past relative sea level evolution (supporting information Text S2), both suggest that the North American ice sheet (NAIS) was probably an important contributor to the MWP-1A with a rate of volume change of about 3 m of global sea level equivalent (mSLE) per century. Towards the end of the Younger Dryas, GLAC-1D also presents a collapse of this ice sheet at a rate of 1.5 mSLE per century. Although this feature of the late deglacial NAIS is absent from ICE-6G_C, using the same glacial isostatic data but including an updated ice sheet model, a recent study (Stuhne & Peltier, 2017) has also suggested that a collapse of the late deglacial NAIS could explain the MWP-1B.

Several mechanisms could explain these large scale ice sheet collapses: i) ice stream surges due to internal thermo-mechanical oscillations (MacAyeal, 1993; Calov et al., 2002); ii) grounding line migration for marine ice sheets (DeConto & Pollard, 2016); or iii) strongly negative surface mass balance due to the surface elevation feedbacks (Gregoire et al., 2012; Abe-Ouchi et al., 2013). To date, only this last process has been used in a modelling study to successfully reproduce the largest deglacial abrupt sea level rise, the MWP-1A, with a so-called saddle collapse mechanism (Gregoire et al., 2012). Surface mass balance processes such as the saddle collapse are enhanced by abrupt warming such as the Bølling-Allerød that was mostly synchronous with the MWP-1A. Unlike surface mass balance processes, once triggered, mechanical instabilities are self-sustained and are only weakly sensitive to any later climate change.

Whilst a fair amount of ice sheet simulations of Northern Hemisphere deglaciation are available in the literature, they were performed with a former generation of ice sheet models that do not account for the complexity of grounding line dynamics (Gregoire et al., 2012; Abe-Ouchi et al., 2013; Charbit et al., 2005; Heinemann et al., 2014; Ganopolski & Brovkin, 2017). Ice sheet models now either use a very high spatial resolution at the ice margin to explicitly solve grounding line dynamics (Larour et al., 2012), in some cases with some sub-grid parametrisations (Winkelmann et al., 2011), or they impose an ice flux crossing the grounding line using analytically derived formulations (Schoof, 2007; Tsai et al., 2015). These newer models have a grounding line migration that is much more sensitive to changes in boundary conditions (mass balance and sea level (Pattyn et al., 2013)) with respect to the previous generation.

2 Methods

In this work, we use the GRISLI ice sheet model (Quiquet, Dumas, et al., 2018) to simulate the evolution of the Northern Hemisphere ice sheets for the last 26 ka. We showed recently that the model was able to correctly reproduce the grounding line migration for the Antarctic ice sheet across the last glacial-interglacial cycles (Quiquet, Dumas, et al., 2018). The ice sheet model accounts for glacial isostasy with an elastic lithosphere - relaxed asthenosphere model. Any topographic depression below the contemporaneous eustatic sea level is assumed to be flooded with a water surface elevation at the eustatic sea level value. The climatic forcing that drives the ice sheet evolution is computed in two completely independent ways. In a first series of experiments the iLOVECLIM climate model (Roche, Dumas, et al., 2014; Roche, Paillard, et al., 2014) is bi-directionally coupled to GRISLI using a new downscaling capability (Quiquet, Roche, et al., 2018) to compute ice sheet surface mass balance from downscaled physical variables at the resolution of the ice sheet model for each atmospheric model time step. Surface mass balance is computed with an insolation - melt model (van den Berg et al., 2008) with local melt parameter tuning to partially correct for the model biases (Heinemann et al., 2014). Sub-shelf melting rate is computed from temperature and salinity provided by the ocean model (Beckmann & Goosse, 2003). The second series of experiments consist of a suite of ice sheet stand-alone experiments forced by an ensemble of synthetic climate histories that are elaborated from general circulation model (GCM) outputs and a proxy for temperature variability deduced from a Greenland ice core (Charbit et al., 2007). In this case, the GCM last glacial maximum anomalies with respect to the pre-industrial from the PMIP3 database (Abe-Ouchi et al., 2015) are added to reanalysis data (Dee et al., 2011). If these stand-alone experiments use an idealised climate forcing that may lack consistency between ice sheet and climate changes, they nonetheless provide an ensemble of alternative ice sheet evolutions during the deglaciation. More details on the modelling setup is given in the supporting information (Text S1).

3 Results

Both sets of experiments produce deglacial NAIS volume losses in general agreement with the geologically-constrained reconstructions (Fig. 1A). However, in detail they do present some important differences. On the one hand, the stand-alone experiments show a pronounced millenial scale variability in ice volume, which is a direct consequence of the imposed atmospheric variability recorded in Greenland ice cores. In particular, the simulated NAIS loses ice up to a rate of 5 mSLE per century (Fig. 1B) in response to the abrupt Bølling warming at 14.6 kaBP. That rate is comparable to the magnitude of the MWP-1A recorded in sea-level archives (Deschamps et al., 2012). These experiments show a second maximum in rate of volume loss towards the end of the Younger Dryas circa 11.5 kaBP, in agreement with the GLAC-1D reconstruction. On the other hand, in the coupled experiment, the gradual change in forcings (orbital and greenhouse gases) leads to a smoother simulated ice volume reduction. While ice volume between 26 and 17 kaBP is relatively stable, after this date, the ice loss rates are overestimated with respect to the geomorphological reconstructions, leading to a smaller simulated ice sheet extent (Fig. S1 and Fig. S2). This faster ice sheet volume reduction in the coupled experiment is in part due to the fact that we do not account for the impact of melt water flux to the ocean which are expected to weaken the North Atlantic overturning circulation and, as a result, to delay the Northern Hemisphere warming. Since the coupled model does not internally produce the Bølling warming, contrary to the stand-alone experiments, it presents only one peak in rates of volume loss circa 13 kaBP of about 2 mSLE per century. We show in the following that the latest acceleration in ice loss, in the two sets of experiments, is due to the large proglacial lake that forms at the southern edge of the NAIS.

The pattern of our modelled NAIS retreat in the coupled experiment is illustrated in Fig. 2 with two selected snapshots; one before and one after the timing of maximum ice loss rate for the coupled experiment. At 13.8 kaBP (before the event, Fig. 2A), the simulated ice sheet reproduces the major ice streams inferred by geomorphological observations (Hudson Strait, Lancaster Sound, Amundsen Gulf (Margold et al., 2018) on Fig. 2). This ice streams are predominantly controlled by bedrock features (valleys, Fig. S3) and terminate in the Atlantic and Arctic oceans. On the contrary, the continental southern margin does not show at this time any well identified ice streams. However, retreat of the ice sheet on its southern margin produced the large proglacial lake Agassiz-Ojibway (Teller, 2003). One thousand years later, at 12.8 kaBP (Fig. 2B), dramatic acceleration of the southern part of the ice sheet is simulated and associated with substantial grounding line retreat. Velocities of grounded ice shift from below 500 m yr^{-1} to about 2000 m yr^{-1}

in the vicinity of the grounding line. In the stand-alone experiments this rapid acceleration in ice sheet velocity is systematically reproduced independently from the climatic forcing, but it occurs later, towards the end of the Younger Dryas (Fig. S4). This rapid ice sheet collapse is due to a mechanism similar to the marine ice sheet instability (Weertman, 1974; Schoof, 2007) except that it occurs in a lake and not in the ocean. In the following, this process will be referred to as proglacial lake ice sheet instability, PLISI.

To better illustrate the mechanism, we show a cross-section of the ice sheet for the same temporal snapshots in Fig. 3. Before the instability initiation, the bedrock under the ice sheet is depressed with respect to its present-day value due to the glacial ice load (Fig. 3A). In the course of the deglaciation, the progressive thinning due to surface mass balance decrease leads eventually to floating conditions and the retrograde bed triggers the PLISI. The grounding line retreats by more than 700 km in the region of Lake Agassiz-Ojibway within one thousand years (Fig. 3B). Once triggered, the mechanism is mostly mechanically driven (supporting information Text S3).

To assess the importance of the PLISI in shaping the deglaciation, we isolate the effect of surface mass balance by preventing the occurrence of the mechanical instability, by assuming that the southern margin of the NAIS is perpetually grounded until 8 kaBP. Excluding lake effects on ice dynamics results in maximal rates of ice loss halved with respect to the experiments in which the PLISI is accounted for (Fig. 4 and Fig. S7). In particular, magnitude of local ice fluxes are divided by 10 in the area of present-day Hudson Bay (Fig. S8). The PLISI is thus a crucial process for the NAIS dynamics and explains the late deglacial acceleration of the ice sheet volume loss.

Since the PLISI is a grounding line instability, its importance is tightly linked to the lake water depth through a flotation criteria. Our ice sheet model does not simulate explicitly proglacial lakes and the lake surface elevation is assumed to follow the eustatic sea level. This is a conservative estimate since at high latitudes the water inputs to the lake exceed the evaporation and the water level is thus controlled by the elevation of the outlet. It is believed that large proglacial lakes at the southern margin of the NAIS presented probably a surface level about 100 metres or more above the contemporaneous eustatic sea level (Lambeck et al., 2017; Clarke et al., 2004). For this reason, we performed additional experiments for which we assume a constant lake surface elevation at +50 m above present-day sea level in the NAIS southern margin area (about +120 m above eustatic sea level at 13 kaBP). In this case, the PLISI is enhanced and it often doubles the maximum ice loss rate compared to the simulations where the mechanism is inhibited (Fig. 4 and Fig. S7). While these additional experiments with a higher lake surface elevation lead to substantial difference in ice loss rates, we made additional computations that suggest that the elevation could be higher than +150 metres above present-day sea-level in the course of the deglaciation (supporting information Text S4). This implies that if more realistic varying lake surface elevations were considered in our experiments, the PLISI would have been reinforced. As such, the implementation of an interactive depression-filling algorithm to infer the lake-water depth (e.g. Berends & Wal, 2016) could be important to implement in ice sheet models to simulate the last deglaciation.

4 Discussion

With a set of model simulations, we have shown that proglacial lakes can greatly influence ice sheet dynamics by providing rapid grounding line retreats. If the magnitude and the timing of this rapid grounding line retreat depends on climate evolution, the instability occurs systematically in the course of the deglaciation as a result of the depressed bedrock resulting from glacial ice load. It is also only weakly sensitive to calving formulation and lake sub-shelf melting rates (supporting information Text S5 and Fig. S9) because of the strongly negative surface mass balance at the NAIS southern margin. In our simulations, the PLISI results in an acceleration of the deglaciation of the

NAIS in its final stage, with rates of volume change of about 2 mSLE per century. The PLISI could be thus responsible of the debated MWP-1B recorded at Barbados (Abdul et al., 2016). Contrary to the MWP-1A, which could be a surface melt response to the abrupt Bølling warming leading to a saddle-collapse (Gregoire et al., 2012), this event is almost entirely mechanically driven although triggered by a decrease in surface mass balance. As such, it is a self-sustained instability that can maintain large ice sheet volume loss regardless of later climate change. The PLISI could explain the fan-like ice streams observed in the geological record at the end of the Younger Dryas (Margold et al., 2018) which also coincide with the MWP-1B.

This mechanism raises a number of scientific questions as we have no contemporaneous analogues, although a large number of glaciers, notably in Patagonia, Greenland and Antarctica, terminate in proglacial lakes (Carrivick & Tweed, 2013). These glaciers are relatively small and do not allow for large floating ice shelves. Instead, the PLISI could have generated large and thick ice shelves floating over freshwater cavities. Since present-day freshwater glaciers show calving and basal melting rates smaller than their tidewater analogues (Benn et al., 2007; Trüssel et al., 2013), large scale sub-shelf refreezing could eventually occur within the cavities. If our experiments are weakly sensitive to calving and sub-shelf melting rates because of the strongly negative surface mass balance at the southern margin of the NAIS during the deglaciation, this might not always be the case for other time periods and/or ice sheets.

If the PLISI mechanism is crucial to understand the deglaciation of the NAIS, it will be as important for the Eurasian ice sheet. Large proglacial lakes were also present at the southern flank of the Eurasian ice sheet, in the vicinity of the Baltic and White seas (Patton et al., 2017). The PLISI could be a mechanism that explains the observed cyclicity in abrupt discharge events recorded in the Black sea (Soulet et al., 2013). More generally, the PLISI could be crucial to understand deglacial Pleistocene eustatic sea level.

While grounding line dynamics is a well established process to account for the Antarctic ice sheet evolution, the PLISI mechanism is another manifestation of its importance for ice sheet dynamics. These results highlight the need for a good understanding of grounding line physics and its representation in numerical models in order to reduce the uncertainties on sea level projections for the ongoing deglaciation.

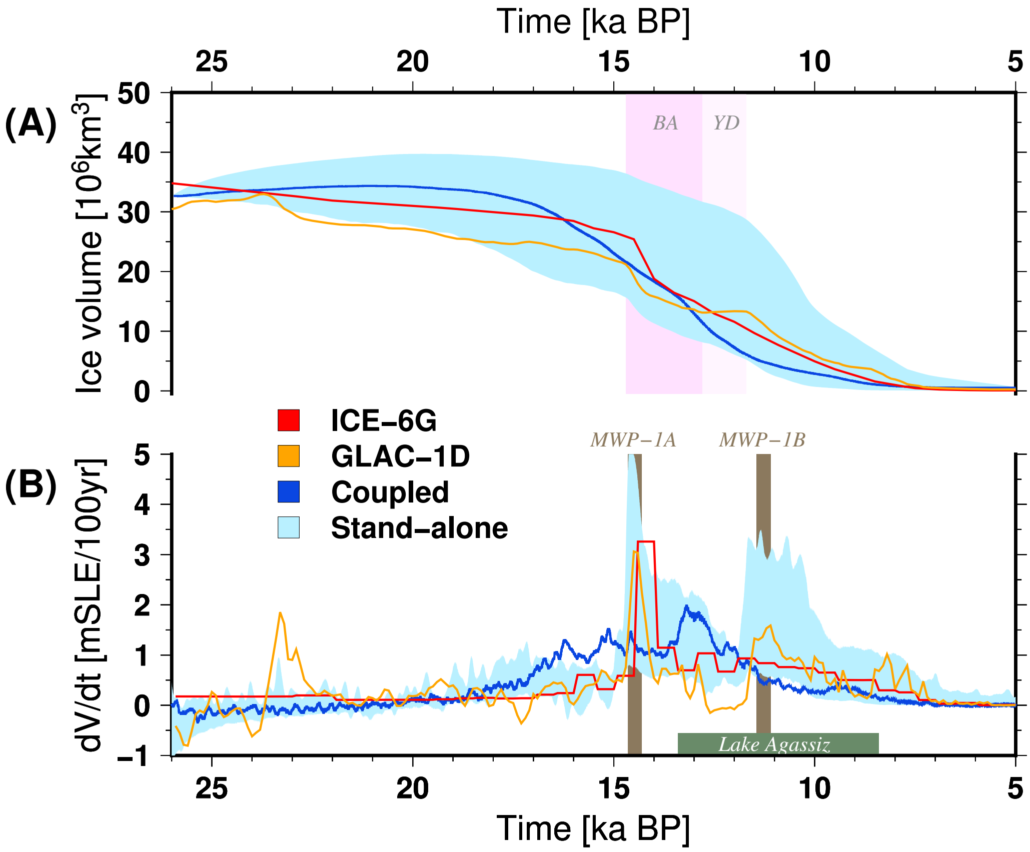

Figure 1. Temporal evolution. Simulated total ice volume (A) and rate of ice loss (expressed as ice volume contributing to sea level rise per century) (B) through the deglaciation (26 kaBP 5 kaBP) for the NAIS. Dark blue depicts the simulated NAIS using the GRISLI-iLOVECLIM set-up while the light blue envelop depicts the spread within the GRISLI stand-alone experiments (Methods). The ice sheet volume and rate of volume change of GLAC-1D and ICE-6G are shown in orange and red, respectively. The Bølling-Allerød warm period and the Younger Dryas cold period are shown by the pink vertical shading. The two melt-water pulses discussed in the text are in brown and the presence of the Lake Agassiz is shown by the horizontal green bar.

Acknowledgments

Archiving of source data of the figures presented in the main text of the manuscript is underway. Data will be made publicly available upon publication of the manuscript on the Zenodo repository with digital object identifier 10.xxxx/zenodo.xxxxxxx. They are temporarily available for review purposes at: https://sharebox.lsce.ipsl.fr/index.php/s/7Aygc0X5Bq3SGx2 (694.9 Mb). The research leading to these results has received funding from the European Research Council under the European Union's Seventh Framework Program (FP7/2007-2013 Grant agreement n 339108).

References

Abdul, N. A., Mortlock, R. A., Wright, J. D., & Fairbanks, R. G. (2016). Younger Dryas sea level and meltwater pulse 1b recorded in Barbados reef crest coral Acropora palmata. *Paleoceanography*, *31*(2), 330–344. doi: 10.1002/2015PA002847

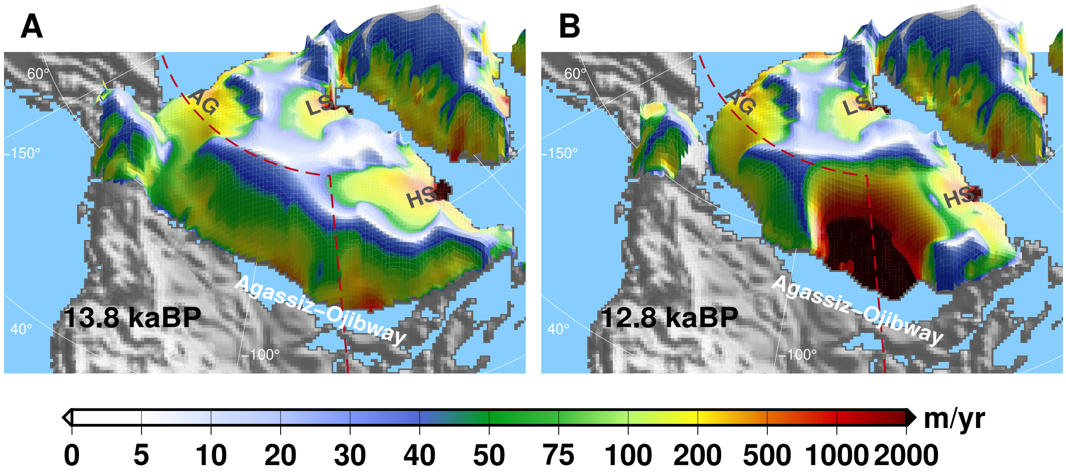

Figure 2. Ice sheet geometry at the time of the instability. Vertically integrated velocity in the coupled experiment for two snapshots, before (A) and after (B) the maximum in rate of ice loss for the NAIS. The two snapshots are separated by one thousand year. For this 3-D perspective plot, the velocity is draped on top of the ice sheet topography. The dashed line stands for the cross-section discussed in the main text. The major simulated ice streams are the Amundsen Gulf (AG), Lancaster Sound (LS) and Hudson Strait (HS) ice streams.

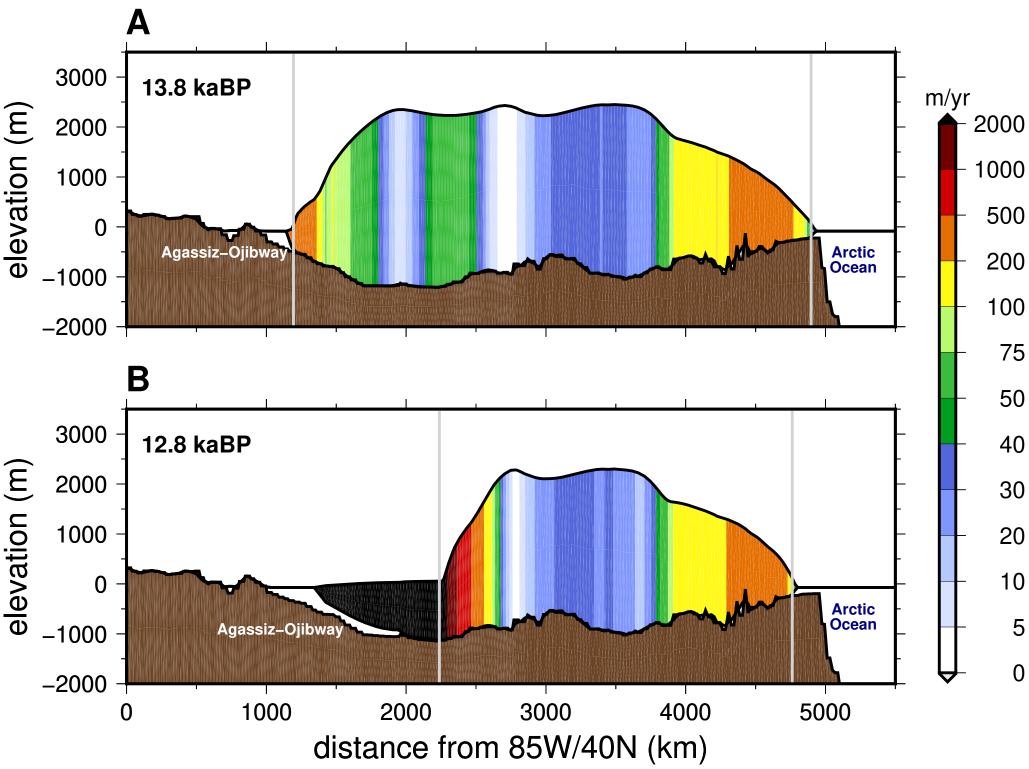

Figure 3. Bedrock profile. Cross-section of the NAIS (dashed line on Fig. 2) in the coupled experiment for two snapshots, before (A) and after (B) the maximum in rate of ice loss. The bedrock is depicted in brown color, the horizontal black line represents the contemporaneous eustatic sea level and the vertically averaged velocity is shown with the color palette. The vertical grey lines represent the position of the grounding line.

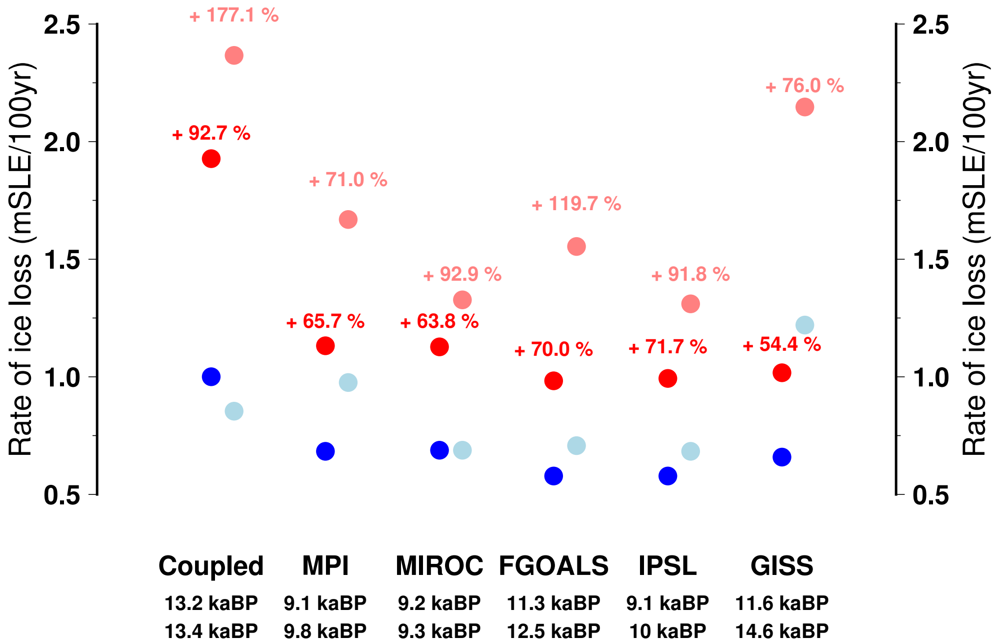

Figure 4. Importance of the lake level for the ice loss. Rate of ice loss towards the maximum of the PLISI event (red dots) and their contemporaneous values when we prevent the PLISI (blue dots) for the coupled model and different stand-alone experiments forced by PMIP3 models (Methods). Light colours represent the experiments in which we assume a lake level higher than the eustatic sea level (prescribed at +50 metres above present-day sea level). Timing of the maximum in rate of ice loss differs for the different lake levels (earlier for higher lake level). The stand-alone experiments here use a weighing factor for the fast variability of 0.25.

Abe-Ouchi, A., Saito, F., Kageyama, M., Braconnot, P., Harrison, S. P., Lambeck, K., ... Takahashi, K. (2015, November). Ice-sheet configuration in the CMIP5/PMIP3 Last Glacial Maximum experiments. *Geoscientific Model Development*, *8*(11), 3621–3637. doi: 10.5194/gmd-8-3621-2015

Abe-Ouchi, A., Saito, F., Kawamura, K., Raymo, M. E., Okuno, J., Takahashi, K., & Blatter, H. (2013). Insolation-driven 100,000-year glacial cycles and hysteresis of ice-sheet volume. *Nature*, *500*(7461), 190–193. doi: 10.1038/nature12374

Barber, D. C., Dyke, A., Hillaire-Marcel, C., Jennings, A. E., Andrews, J. T., Kerwin, M. W., ... Gagnon, J.-M. (1999, July). Forcing of the cold event of 8,200 years ago by catastrophic drainage of Laurentide lakes. *Nature*, *400*(6742), 344–348. doi: 10.1038/22504

Bard, E., Hamelin, B., Deschamps, P., & Camoin, G. (2016). Comment on "Younger Dryas sea level and meltwater pulse 1b recorded in Barbados reefal crest coral Acropora palmata" by N. A. Abdul et al. *Paleoceanography*, *31*(12), 1603–1608. doi: 10.1002/2016PA002979

Beckmann, A., & Goosse, H. (2003). A parameterization of ice shelfocean interaction for climate models. *Ocean Modelling*, *5*(2), 157–170. doi: 10.1016/S1463-5003(02)00019-7

Benn, D. I., Warren, C. R., & Mottram, R. H. (2007, June). Calving processes and the dynamics of calving glaciers. *Earth-Science Reviews*, *82*(3), 143–179. doi: 10.1016/j.earscirev.2007.02.002

Berends, C. J., & Wal, R. S. W. v. d. (2016, December). A computationally efficient depression-filling algorithm for digital elevation models, applied to proglacial lake drainage. *Geoscientific Model Development*, *9*(12), 4451–4460. doi: 10.5194/gmd-9-4451-2016

Calov, R., Ganopolski, A., Petoukhov, V., Claussen, M., & Greve, R. (2002, December). Large-scale instabilities of the Laurentide ice sheet simulated in a fully coupled climate-system model. *Geophysical Research Letters*, *29*(24), 2216. doi: 10.1029/2002GL016078

Carrivick, J. L., & Tweed, F. S. (2013). Proglacial lakes: character, behaviour and geological importance. *Quaternary Science Reviews*, *78*, 34–52. doi: 10.1016/j.quascirev.2013.07.028

Charbit, S., Kageyama, M., Roche, D., Ritz, C., & Ramstein, G. (2005, October). Investigating the mechanisms leading to the deglaciation of past continental northern hemisphere ice sheets with the CLIMBER GREMLINS coupled model. *Global and Planetary Change*, *48*, 253–273.

Charbit, S., Ritz, C., Philippon, G., Peyaud, V., & Kageyama, M. (2007, January). Numerical reconstructions of the Northern Hemisphere ice sheets through the last glacial-interglacial cycle. *Climate of the Past*, *3*, 15–37.

Clarke, G. K. C., Leverington, D. W., Teller, J. T., & Dyke, A. S. (2004, February). Paleohydraulics of the last outburst flood from glacial Lake Agassiz and the 8200BP cold event. *Quaternary Science Reviews*, *23*(3), 389–407. doi: 10.1016/j.quascirev.2003.06.004

DeConto, R. M., & Pollard, D. (2016). Contribution of Antarctica to past and future sea-level rise. *Nature*, *531*(7596), 591. doi: 10.1038/nature17145

Dee, D. P., Uppala, S. M., Simmons, A. J., Berrisford, P., Poli, P., Kobayashi, S., ... Vitart, F. (2011, April). The ERA-Interim reanalysis: configuration and performance of the data assimilation system. *Quarterly Journal of the Royal Meteorological Society*, *137*(656), 553–597. doi: 10.1002/qj.828

Deschamps, P., Durand, N., Bard, E., Hamelin, B., Camoin, G., Thomas, A. L., ... Yokoyama, Y. (2012). Ice-sheet collapse and sea-level rise at the Bølling warming 14,600 years ago. *Nature*, *483*(7391), 559. doi: 10.1038/nature10902

Fowler, A. C., Rickaby, R. E. M., & Wolff, E. W. (2013, November). Exploration of a simple model for ice ages. *GEM - International Journal on Geomathematics*,

4(2), 227–297. doi: 10.1007/s13137-012-0040-7
Ganopolski, A., & Brovkin, V. (2017). Simulation of climate, ice sheets and CO2 evolution during the last four glacial cycles with an Earth system model of intermediate complexity. *Clim. Past*, *13*(12), 1695–1716. doi: 10.5194/cp-13-1695-2017
Gregoire, L. J., Payne, A. J., & Valdes, P. J. (2012). Deglacial rapid sea level rises caused by ice-sheet saddle collapses. *Nature*, *487*(7406), 219. doi: 10.1038/nature11257
Heinemann, M., Timmermann, A., Elison Timm, O., Saito, F., & Abe-Ouchi, A. (2014). Deglacial ice sheet meltdown: orbital pacemaking and CO2 effects. *Clim. Past*, *10*(4), 1567–1579. doi: 10.5194/cp-10-1567-2014
Hostetler, S. W., Bartlein, P. J., Clark, P. U., Small, E. E., & Solomon, A. M. (2000, May). Simulated influences of Lake Agassiz on the climate of central North America 11,000 years ago. *Nature*, *405*(6784), 334–337. doi: 10.1038/35012581
Ivanovic, R. F., Gregoire, L. J., Kageyama, M., Roche, D. M., Valdes, P. J., Burke, A., … Tarasov, L. (2016). Transient climate simulations of the deglaciation 21–9 thousand years before present (version 1) PMIP4 Core experiment design and boundary conditions. *Geoscientific Model Development*, *9*(7), 2563–2587. doi: 10.5194/gmd-9-2563-2016
Krinner, G., Mangerud, J., Jakobsson, M., Crucifix, M., Ritz, C., & Svendsen, J. I. (2004, January). Enhanced ice sheet growth in Eurasia owing to adjacent ice-dammed lakes. *Nature*, *427*(6973), 429–432. doi: 10.1038/nature02233
Lambeck, K., Purcell, A., & Zhao, S. (2017, February). The North American Late Wisconsin ice sheet and mantle viscosity from glacial rebound analyses. *Quaternary Science Reviews*, *158*, 172–210. doi: 10.1016/j.quascirev.2016.11.033
Lambeck, K., Rouby, H., Purcell, A., Sun, Y., & Sambridge, M. (2014). Sea level and global ice volumes from the Last Glacial Maximum to the Holocene. *Proceedings of the National Academy of Sciences*, *111*(43), 15296. doi: 10.1073/pnas.1411762111
Larour, E., Seroussi, H., Morlighem, M., & Rignot, E. (2012, March). Continental scale, high order, high spatial resolution, ice sheet modeling using the Ice Sheet System Model (ISSM). *Journal of Geophysical Research: Earth Surface*, *117*(F1), F01022. doi: 10.1029/2011JF002140
Liu, J., Milne, G. A., Kopp, R. E., Clark, P. U., & Shennan, I. (2016, February). Sea-level constraints on the amplitude and source distribution of Meltwater Pulse 1a. *Nature Geoscience*, *9*(2), 130–134. doi: 10.1038/ngeo2616
MacAyeal, D. R. (1993). Binge/purge oscillations of the Laurentide Ice Sheet as a cause of the North Atlantic's Heinrich events. *Paleoceanography*, *8*(6), 775–784. doi: 10.1029/93PA02200
Margold, M., Stokes, C. R., & Clark, C. D. (2018, June). Reconciling records of ice streaming and ice margin retreat to produce a palaeogeographic reconstruction of the deglaciation of the Laurentide Ice Sheet. *Quaternary Science Reviews*, *189*, 1–30. doi: 10.1016/j.quascirev.2018.03.013
Patton, H., Hubbard, A., Andreassen, K., Auriac, A., Whitehouse, P. L., Stroeven, A. P., … Hall, A. M. (2017, August). Deglaciation of the Eurasian ice sheet complex. *Quaternary Science Reviews*, *169*, 148–172. doi: 10.1016/j.quascirev.2017.05.019
Pattyn, F., Perichon, L., Durand, G., Favier, L., Gagliardini, O., Hindmarsh, R. C. A., … Wilkens, N. (2013). Grounding-line migration in plan-view marine ice-sheet models: results of the ice2sea MISMIP3d intercomparison. *Journal of Glaciology*, *59*(215), 410–422. doi: 10.3189/2013JoG12J129
Peltier, W. R., Argus, D. F., & Drummond, R. (2015). Space geodesy constrains ice age terminal deglaciation: The global ICE-6G_c (VM5a) model. *Journal of Geophysical Research: Solid Earth*, *120*(1), 450–487. doi:

10.1002/2014JB011176
Pollard, D. (1982, March). A simple ice sheet model yields realistic 100 kyr glacial cycles. *Nature*, *296*(5855), 334–338. doi: 10.1038/296334a0
Quiquet, A., Dumas, C., Ritz, C., Peyaud, V., & Roche, D. M. (2018, dec). The GRISLI ice sheet model (version 2.0): calibration and validation for multi-millennial changes of the Antarctic ice sheet. *Geoscientific Model Development*, *11*(12), 5003–5025. doi: 10.5194/gmd-11-5003-2018
Quiquet, A., Roche, D. M., Dumas, C., & Paillard, D. (2018, feb). Online dynamical downscaling of temperature and precipitation within the *i*LOVECLIM model (version 1.1). *Geoscientific Model Development*, *11*(1), 453–466. doi: 10.5194/gmd-11-453-2018
Roche, D. M., Dumas, C., Bügelmayer, M., Charbit, S., & Ritz, C. (2014, July). Adding a dynamical cryosphere to iLOVECLIM (version 1.0): coupling with the GRISLI ice-sheet model. *Geosci. Model Dev.*, *7*(4), 1377–1394. doi: 10.5194/gmd-7-1377-2014
Roche, D. M., Paillard, D., Caley, T., & Waelbroeck, C. (2014, December). LGM hosing approach to Heinrich Event 1: results and perspectives from datamodel integration using water isotopes. *Quaternary Science Reviews*, *106*, 247–261. doi: 10.1016/j.quascirev.2014.07.020
Schoof, C. (2007). Ice sheet grounding line dynamics: Steady states, stability, and hysteresis. *Journal of Geophysical Research (Earth Surface)*, *112*.
Soulet, G., Ménot, G., Bayon, G., Rostek, F., Ponzevera, E., Toucanne, S., … Bard, E. (2013, April). Abrupt drainage cycles of the Fennoscandian Ice Sheet. *Proceedings of the National Academy of Sciences*, *110*(17), 6682–6687. doi: 10.1073/pnas.1214676110
Stuhne, G. R., & Peltier, W. R. (2017). Assimilating the ICE-6G_c Reconstruction of the Latest Quaternary Ice Age Cycle Into Numerical Simulations of the Laurentide and Fennoscandian Ice Sheets. *Journal of Geophysical Research: Earth Surface*, *122*(12), 2324–2347. doi: 10.1002/2017JF004359
Tarasov, L., Dyke, A. S., Neal, R. M., & Peltier, W. R. (2012, January). A data-calibrated distribution of deglacial chronologies for the North American ice complex from glaciological modeling. *Earth and Planetary Science Letters*, *315-316*, 30–40. doi: 10.1016/j.epsl.2011.09.010
Teller, J. T. (1995). History and drainage of large ice-dammed lakes along the Laurentide Ice Sheet. *Quaternary International*, *28*, 83–92. doi: 10.1016/1040-6182(95)00050-S
Teller, J. T. (2003, January). Controls, history, outbursts, and impact of large late-Quaternary proglacial lakes in North America. In *Developments in Quaternary Sciences* (Vol. 1, pp. 45–61). Elsevier. doi: 10.1016/S1571-0866(03)01003-0
Teller, J. T., & Leverington, D. W. (2004, May). Glacial Lake Agassiz: A 5000 yr history of change and its relationship to the δ18O record of Greenland. *GSA Bulletin*, *116*(5-6), 729–742. doi: 10.1130/B25316.1
Trüssel, B. L., Motyka, R. J., Truffer, M., & Larsen, C. F. (2013). Rapid thinning of lake-calving Yakutat Glacier and the collapse of the Yakutat Icefield, southeast Alaska, USA. *Journal of Glaciology*, *59*(213), 149–161. doi: 10.3189/2013J0G12J081
Tsai, V. C., Stewart, A. L., & Thompson, A. F. (2015). Marine ice-sheet profiles and stability under Coulomb basal conditions. *Journal of Glaciology*, *61*(226), 205–215. doi: 10.3189/2015JoG14J221
van den Berg, J., van de Wal, R., & Oerlemans, H. (2008, April). A mass balance model for the Eurasian Ice Sheet for the last 120,000years. *Global and Planetary Change*, *61*(3), 194–208. doi: 10.1016/j.gloplacha.2007.08.015
Weertman, J. (1974). Stability of the Junction of an Ice Sheet and an Ice Shelf. *Journal of Glaciology*, *13*(67), 3–11. doi: 10.3189/S0022143000023327
Wiersma, A. P., & Renssen, H. (2006, January). Modeldata comparison for

the 8.2kaBP event: confirmation of a forcing mechanism by catastrophic drainage of Laurentide Lakes. *Quaternary Science Reviews*, *25*(1), 63–88. doi: 10.1016/j.quascirev.2005.07.009

Winkelmann, R., Martin, M. A., Haseloff, M., Albrecht, T., Bueler, E., Khroulev, C., & Levermann, A. (2011, September). The Potsdam Parallel Ice Sheet Model (PISM-PIK) Part 1: Model description. *The Cryosphere*, *5*(3), 715–726. doi: 10.5194/tc-5-715-2011

Supporting Information for "Deglacial ice sheet instabilities induced by proglacial lakes"

Aurélien, Quiquet[1], Christophe, Dumas[1], Didier, Paillard[1],Gilles, Ramstein[1], Catherine, Ritz[2], Didier M., Roche[1,3]

[1]Laboratoire des Sciences du Climat et de l'Environnement, LSCE/IPSL, CEA-CNRS-UVSQ, Université Paris-Saclay, F-91191 Gif-sur-Yvette, France

[2]Université Grenoble Alpes, CNRS, IRD, Grenoble INP, IGE, 38000 Grenoble, France

[3]Vrije Universiteit Amsterdam, Faculty of Science, Cluster Earth and Climate, de Boelelaan 1085, 1081HV Amsterdam, The Netherlands

Contents of this file

1. Text S1 to S6
2. Figures S1 to S11

Corresponding author: A. Quiquet, Laboratoire des Sciences du Climat et de l'Environnement, LSCE/IPSL, CEA-CNRS-UVSQ, Université Paris-Saclay, F-91191 Gif-sur-Yvette, France (aurelien.quiquet@lsce.ipsl.fr)

Introduction

This supplement contains additional material on our model experiments. Text S1 provides further information on the methods used. Text S2 discusses simulated ice sheet evolution agreement with geologically-constrained reconstructions and timing of the proglacial lake ice sheet instability. Text S3 quantifies the respective role of surface and basal mass balance with respect to ice discharge. Text S4 and S5 provides more information on the lake water depth and on the sensitivity of the ice sheet instability to sub-shelf melting and calving rates. Finally Text S6 is a discussion on the role of the millenial atmospheric variability in the stand-alone experiments. Fig. S1 to S11 are additional figures to expend the analyses of the main text and the discussions raised in the this supporting information.

Text S1. Extended descriptions of methods

Ice sheet model

The ice model used in this study is GRISLI v2 (Quiquet, Dumas, et al., 2018). This model is a recently updated version of the GRISLI model which has been extensively used to study ice and climate interactions for a variety of scientific questions across timescales and in particular for Pleistocene Northern Hemisphere ice sheets. GRISLI is a thermo-mechanically coupled model that uses a combination of the shallow shelf and shallow ice approximations. The sub-grid position of the grounding line is computed with a linear interpolation of the flotation criteria (the difference between the ice load and the buoyancy force). The analytical ice flux at the grounding line (Tsai et al., 2015) is linearly interpolated to the neighbouring velocity grid points. Calving at the ice shelf front is based on a simple cut-off thickness threshold of 250 metres below which ice is calved. Glacial isostasy is accounted for with an elastic lithosphere - relaxed asthenosphere model. Any grid point falling below the contemporaneous eustatic sea level is assumed to be flooded with a water surface elevation at the eustatic sea level value. For the work presented here, we use a 40-km Cartesian grid covering the Northern Hemisphere. For model calibration, we performed a model parameter tuning in which we sampled out four critical parameters (shallow ice enhancement factor, basal drag coefficient, till conductivity for the sub-glacial hydrology model and sub-shelf basal melting rates) with a latin hypercube (Quiquet, Dumas, et al., 2018) of 300 ensemble members. We assumed that the parameters yielded for Antarctica are valid for the Northern Hemisphere ice sheets and we selected the ensemble member that has the lowest root mean square error with respect to the present-day observed Antarctic topography. Unlike Quiquet, Dumas, et al. (2018) we use a present-day Northern Hemisphere sediment thickness distribution to locally enhance basal sliding. Where the sediment thickness is greater than 200 metres, we apply a dimensionless factor of 0.05 to the basal drag coefficient. This is consistent with our knowledge of basal sliding (facilitated over water-saturated till) and ensures a reasonable simulated ice volume at the last glacial maximum (LGM), with an in ice volume difference lower than 10% with respect to ICE-6G_C. Bedrock topography is taken from ETOPO1 and the geothermal heat flux is spatially variable. Both are regridded to the 40-km grid using bilinear interpolation.

Coupled experiments

We used the coupled iLOVECLIM-GRISLI model (Roche, Dumas, et al., 2014). The core of the iLOVECLIM climate model consists of a spectral T21 atmospheric model (EC-Bilt), a vegetation model (VECODE) and a sea ice and 3D free surface ocean (CLIO). Since Roche, Dumas, et al. (2014), the coupling with the ice sheet model has been improved in several important ways. While the surface mass balance was computed with a positive degree day model from bilinearly interpolated atmospheric fields, we now make use of a downscaling scheme (Quiquet, Roche, et al., 2018) to compute a surface mass balance at each atmospheric model time step, using an insolation-temperature-melt model (ITM) (van den Berg et al., 2008). We use absolute fields, namely surface mass balance and near-surface air temperature, without bias correction to force the ice sheet model. In addition, for floating ice shelves, instead of using an ad-hoc prescribed sub-shelf basal melting rate, we compute the melt from temperature and salinity provided by the ocean model (Beckmann & Goosse, 2003). Since the ice sheet model does not distinguish the lakes from the ocean, floating ice grid points that fall outside the oceanic domain, use the nearest oceanic condition to compute sub-shelf melting. This is an important simplification as the lake thermodynamics in lakes is largely different from the one in the ocean (Benn et al., 2007). For this reason, we use a wide range of sub-shelf melting rate and calving threshold and show only a very limited change on the results (supporting information, Fig. S9). Although the model is computationally cheaper than complex general circulation model, our setup requires a substantial amount of time to compute the whole deglaciation, as we require 24 hours to compute approximatively 500 years using 8 processors on our local cluster. For this reason, we use an acceleration factor of 10 for the external forcings (greenhouse gases and orbital configuration). The ice sheet model is run 10 years for 1 year of climate and the coupling frequency is 1. With this setup, the mass conservation of water between the ice sheet model and the rest of the climate model cannot be preserved and as such the hydrological budget is computed without considering the effect of the ice sheet. This prevents the eventual feedbacks between ice sheet volume reduction and Atlantic meridional overturning circulation (AMOC) and the related non-linearities of the climate evolution through the deglaciation. For example, in our experiment we have a deep and active AMOC at the last glacial maximum (~17 Sv, with 1 Sv = 10^6 m^3 s^{-1}) that gradually slows down by 30% towards its Holocene values (~12 Sv). The ITM model has a largely unconstrained free parameter (constant c in van den Berg et al. (2008)). With a homogeneous value of this constant, the NAIS retreats systematically before the Eurasian ice sheet. This temporal mismatch is probably the result of atmospheric biases in the iLOVECLIM model that presents a substantial excessive warmth over North America and a moderate cold bias in the Kara-Barents region for the present-day simulated climate (Heinemann et al., 2014). For this reason we use a geographically variable value for the constant c (varying from about -80 W m^{-2} around present-day Hudson Bay to 0 W m^{-2} in the Kara Sea), based on the present-day temperature bias with respect to ERA-interim (Dee et al., 2011). In order to avoid initial model drift, the following methodology was used:

i- We run first iLOVECLIM for 5000 years under LGM boundary conditions (greenhouse gases and orbital forcing) and with prescribed ice sheets of GLAC-1D. We use the last hundred years of this simulation to generate climatological surface mass balance and surface temperature forcings needed by the ice sheet model.

ii- Using these forcing fields, the ice sheet model is run offline for 100 ka to reach equilibrium.

iii- Finally, we use the spun-up climate (after the 5000 years) of step i as an initial conditions for our deglacial simulations, replacing the GLAC-1D ice sheets by the spun-up ice sheets of ii.

In the climate model, the bathymetry is left unchanged in our experiments. We used a last glacial maximum bathymetry from a previous study (Roche, Paillard, et al., 2014).

Ice sheet stand-alone experiments

For stand-alone experiments we use a simple index method (Charbit et al., 2007). We computed LGM climate anomalies with respect to the pre-industrial from general circulation model outputs of the PMIP3 database (Abe-Ouchi et al., 2015). For the LGM, the monthly near-surface air temperature differences are added on top of the ERA-interim (Dee et al., 2011) 1989-2008 monthly climatologies. Similarly, the monthly precipitation ratio is multiplied by the monthly total precipitation of the 1989-2008 climatology. As in Charbit et al. (2007), the LGM climate anomalies are weighted in time so that the climate forcing for the present-day is entirely the result of the ERA-interim forcing field:

$$\Delta X\left(t\right) = \left(1 - \alpha\left(t\right)\right) \Delta X_{LGM} \tag{1}$$

with X being monthly temperature or total precipitation and α the time dependent glacial index (0 at the LGM and 1 at 0 kaBP). However, while in Charbit et al. (2007) the glacial index α was purely linear in time, for this work an additional term that accounts for the fast atmospheric variability recorded as in ice cores is used:

$$\alpha(t) = r \times \xi(t) + (1 - r) \times \zeta(t) \tag{2}$$

with ξ which follows the North GRIP δ^{18}O and which is scaled so it is 0 at the LGM and 1 at 0 kaBP. The slow orbital variability, ζ , is simply the time from the LGM, with a value of 0 for the LGM at 21 kaBP and 1 at 0 kaBP. The weighting factor, r, is an unknown parameter which has important consequences on the imposed climatic scenarios. In addition, it is a simplification to assume atmospheric synchronicity and similar amplitude of changes between the Greenland and North America ice sheets. For this reason, for a given GCM climate forcing, we run various possibilities for r: 0.15, 0.25, 0.35, 0.45 and 0.55 (a high value meaning that more importance is given to rapid, millenial, variability with respect to orbital variability, Fig. S10). The reference value for the figures shown in the manuscript is 0.25, which corresponds to a limited importance of the fast variability, with a transition from the LGM to the pre-industrial almost linear (Fig. S10). The rapid variability tends to accelerate the ice loss and produces larger MWP-1A event. However, in this case, even though the event happens earlier in the deglaciation (Fig. S10), the PLISI continues to play a crucial role when flotation is reached at the southern margin of the ice sheet. We also use a constant and homogeneous vertical lapse rate of 6 °C km^{-1} to account for temperature changes due to topography changes. Precipitation is corrected using the same temperature-precipitation relationship as in Charbit et al. (2007). From the various GCM outputs in the PMIP3 database, we selected the five that produce reasonable ice sheet geometries at the LGM: FGOALS-g2, IPSL-CM5A-LR, MPI-ESM-P, MIROC-ESM and GISS-E2-R. Other climate forcings in the PMIP3 database produced too small ice sheets (e.g. CNRM-CM5 or MRI-CGCM3). The surface mass balance is computed with a positive degree day model. For the oceanic forcing we use a two value sub-shelf basal melting rate (continental shelf, 0.2 m yr^{-1}, and deep ocean, 10 m yr^{-1} under present-day conditions) perturbed by an index for the strength of the AMOC calculated from a North Atlantic benthic foraminifera record (Quiquet, Dumas, et al., 2018). Similarly to the coupled simulations, the initial ice sheet conditions for the stand-alone experiments are the spun-up ice sheets from the equilbrium simulations under perpetual LGM climatic forcing field computed from iLOVECLIM. The simulations are transient and span the last 26 ka.

Text S2. Agreement with geologically-constrained reconstructions and timing of the event

Our knowledge of individual ice volume for the different ice sheets across the last deglaciation is mostly known from comprehensive inverse methods applied to indicators for modern surface subsidence measurements and radiocarbon dated archives for relative sea level evolution. Two major reconstructions are publicly available in the literature. The ICE-6G_C VM5a model (ICE-6G_C in the manuscript)(Peltier et al., 2015) makes use of the most complete dataset used to constrain the local ice thickness history while the global ice mass is constrained by eustatic sea level curves. The GLAC-1D model (Tarasov et al., 2012; Ivanovic et al., 2016) is a compilation of various works and it differs from ICE-6G_C by the inclusion of a comprehensive ice sheet model and fewer degrees of freedom in the inversion procedure. If the two reconstructions agree generally very well with respect to the ice extent history, the ice volume is nonetheless largely different. For the NAIS, there is more than 5 million cubic kilometres (more than 10 metres of sea level equivalent) of ice volume difference between the two reconstructions. The GLAC-1D model shows a lower ice volume and a thinner ice sheet for the LGM. The transient evolution is also very different. Thus, if both reconstructions suggest a NAIS contribution to the MWP-1A of about 3 m of global sea level equivalent (mSLE) per century, they disagree for the latest stage of the deglaciation. The ICE-6G_C reconstruction shows a gradual ice volume reduction after 14 kaBP while GLAC-1D shows a pause in ice loss during the Younger Dryas and two pulses (between 12 and 11 kaBP and later between 9 and 8 kaBP). Towards the end of the Younger Dryas, GLAC-1D shows a NAIS collapse at a rate of 1.5 mSLE. Although this feature of the late deglacial NAIS is absent from ICE-6G_C, using the same glacial isostatic data but including an updated ice sheet model, a recent study (Stuhne & Peltier, 2017) has also suggested that a collapse of the late deglacial NAIS could explain the MWP-1B. These differences between two geophysically-constrained reconstructions are due to a poor understanding of the Earth rheology and its spatial and temporal evolution but also to some different interpretations of archives for relative sea level changes. Our approach is drastically different since it does not involve any inversion of palaeo-data and as such there is no a priori on the relative importance of the different processes.

The simulated ice sheet extent topography for the last glacial maximum (21 kaBP) in the coupled experiment is shown in Fig. S1. The extent is in generally good agreement with the geophysically-constrained reconstructions of ICE-6G_C and GLAC-1D, except in western Eurasia where it is underestimated. The spun-up ice sheet used as initial conditions for our transient experiments was obtained after a long (100 ka) ice sheet simulation under perpetual LGM climate forcing provided by iLOVECLIM. It shows a good agreement in term of volume with both geophysically-constrained reconstructions. However, the coupling that starts at 26 kaBP induces a slight volume increase from 26 kaBP to 21 kaBP, in contradiction with ICE-6G_C and GLAC-1D that show a volume reduction within this time frame. Because the extent is almost unchanged from 26 to 21 kaBP in our coupled simulation, this means that our simulated ice sheet is getting thicker, increasing the mismatch with the two reconstructions. Later in the deglaciation the iLOVECLIM-GRISLI setup produces overestimated melt rates which lead to an underestimation of the ice extent of the NAIS, especially at its southern margin (Fig. S2). This is in part related to the warm bias in the model over North America(Heinemann et al., 2014) and also because there is no feedback of ice sheet volume reduction on North Atlantic overturning circulation. This too early deglaciation introduces a temporal mismatch between the geophysically-constrained reconstructions and the model results, the latter showing a lead of more than 2000 years in some places. As such the coupled simulations offer a weak constraint on the timing of the PLISI, except that its occurrence requires a reduced ice sheet in order to reach the flotation criterion. The stand-alone experiments generally show a much better temporal agreement with the geophysically-constrained reconstructions since in this case the climatic temporal evolution is partly driven by the Greenland temperature variation reconstruction. However, even amongst the stand-alone experiments, the different GCMs produce drastically different NAIS ice sheet evolutions.

Since the PLISI is initially triggered by the floatation criterion, the sensitivity of the simulated NAIS geometry evolution to the climate forcing explains the diversity in terms of timing of the event, which can be as early as 13.8 kaBP to as late as 9.6 kaBP (Fig. S4). Given these uncertainties in term of forcings and ice sheet geometry evolution, the model experiments only offer a weak constraints on the timing of the PLISI. Nonetheless, to happen it requires a reduce ice sheet size (to reach floatation). The experiments that have the best agreement with the geophysically-constrained reconstructions tend to show a PLISI happening between 9 and 11 kaBP.

Text S3. Respective role of surface and basal mass balance with respect to ice discharge

The study of the different terms of the mass conservation equation can help us to quantify the respective role of mass balance induced by climate change and mass balance that results from ice discharge. The mass conservation equation is the following:

$$\frac{\partial H}{\partial t} = B - \nabla\left(\boldsymbol{u}H\right) \tag{3}$$

where H is the ice thickness, B is the sum of the surface and basal mass balance and $\boldsymbol{u}$ is the horizontal velocity (i.e. $\nabla\left(\boldsymbol{u}H\right)$ is the ice divergence).

Fig. S5 shows the breakdown of the different terms of Eq. 3 for two snapshots that encompass the maximum rate of volume change in the coupled simulation. Before the event, the melt at the southern margin (Fig. S5a) is partly compensated by the ice flux convergence (Fig. S5b) and the pattern of ice thickness change (Fig. S5c) resembles the one of surface and basal mass balance. Once the PLISI is triggered, the large ice thinning in the vicinity of the proglacial lake grounding line (Fig. S5f) is almost entirely explained by the increased ice flux divergence (Fig. S5e). This shows that if the event is initially triggered by a decrease in surface mass balance, it is nonetheless almost entirely mechanically driven and, as such, independent from any later climate change.

Text S4. Proglacial lake water depth

Since the proglacial lake ice sheet instability is a grounding line instability its trigger is strongly dependent on the water depth at the grounded margin. The accurate modelling of proglacial lakes requires a very high resolution of the palaeo-topography to compute a precise routing of melt-water. It also requires a high confidence in the simulated palaeo-topography since departures from observational ice sheet extent can drastically change the route for melt water. Given the diversity in simulated palaeo-topographies (e.g. Fig. S4) an interactive scheme for proglacial lakes will produce a wide range of lake surface elevations. However, a recent attempt to interactively compute proglacial lake drainage has been made in a large scale ice sheet model with promising results(Berends & Wal, 2016).

Our ice sheet model does not yet simulate explicitly proglacial lakes. In the standard version of the model, any depression below the contemporaneous eustatic sea level is considered flooded with a surface elevation being at the eustatic sea level. This is in fact a conservative estimate since the hydrological budget of these mid- to high-latitude lakes was probably positive and, as such, their surface elevation will be equal to the topographic barrier along the route towards the ocean. With this conservative estimate, we systematically produce a grounding line instability (Fig. S4). Any more realistic changes in lake level in the course of the deglaciation would result in a larger ice sheet volume reduction due to the PLISI. To infer a more realistic value for the lake surface elevation consistent with our modelling results, we built for this paper a depression-filling algorithm. This algorithm computes a connectivity graph that minimises the topographic barrier that separates two given points. We run the algorithm for one snapshot within the deglaciation and selecting one point in the proglacial lake and one in the Atlantic ocean. For the palaeo-topography, we use a North American subset of the ETOPO1 digital elevation model in which we superpose the simulated anomaly with respect to the present-day topography. The outputs of our algorithm is shown in Fig. S6. We found a lake surface elevation at about 160 m above present-day sea level, which is about 235 m above the contemporaneous eustatic sea level, a value close to what has been found in other studies(Clarke et al., 2004). This difference with respect to the coeval sea level is substantial and would have an impact of the magnitude of the PLISI. With additional sensitivity experiments in which we assume a constant lake surface elevation at +50 m above present-day sea level, we considerably amplify the importance of the PLISI (Fig. S7 and Fig. S8) and we expect an even more amplified effect with +160 m above present-day sea level as found in our depression-filling algorithm.

Text S5. Calving events and sub-shelf melt rates in proglacial lakes

The proglacial lake ice sheet instability mechanism leads to a massive solid ice discharge into the lake. While in Antarctica ice shelf thinning and associated calving are mostly controlled by the oceanic thermal forcing, proglacial lakes may remain relatively cold throughout the year with a limited available heat to melt the ice shelves(Trüssel et al., 2013). In addition, present-day freshwater calving glaciers display lower calving rates than their tidewater analogues(Benn et al., 2007). Using different simulations for which we drastically reduce the calving rate, we show that the volume of the ice shelves is not much larger than in the standard experiment and that the grounded ice volume is virtually not changed (Fig. S9). This is because surface mass balance at the southern margin of the ice sheet is strongly negative (surface ablation of several metres per year) and does not allow maintaining an ice shelf (surface ablation greater than ice flux convergence). As a result, calving of the ice at the front plays only a minor role and our experiments are weakly sensitive to its representation in the model. Similarly, we have also performed experiments in which we reduce the sub-shelf basal melting rates and we arrive at the same conclusions (Fig. S9). The predominant role of surface melt in our experiments with respect to sub-glacial processes is a major difference with the dynamics of present-day Antarctic ice shelves.

We need to acknowledge, however, that for different time intervals and/or ice sheets presenting a colder climate with more limited ice ablation at the surface, the effect of sub-shelf melting and calving might be more important. In which case, a specific lake model could be envisioned.

Text S6. Role of the millenial atmospheric variability in the stand-alone experiments

Contrary to the coupled experiment, most of the stand-alone experiments show an important acceleration of ice volume loss at the time of the Bølling warming, which coincides with the MWP-1A. This result is a direct consequence of the methodology chosen for the stand-alone experiments in which the abrupt warming recorded in Greenland is used to compute the temperature change over the NAIS. However, the synchronicity and amplitude of temperature change over the Greenland ice sheet and the NAIS is questionable. The weighting factor r (see methods) is used to modify the importance given to the millenial atmospheric variability recorded in Greenland: for an extreme value of 1 the temperature changes over the NAIS are entirely driven by the Greenland record whereas for a value of 0 there is a linear transition from the last glacial maximum to the pre-industrial forcing. Fig. S10 shows the rate of ice loss for different values of this atmospheric variability weighing factor r for a given GCM forcing (the associated glacial index is shown in Fig. S11). For greater values, there is an important ice sheet collapse during the Bølling warming while for smaller values the deglaciation is smoother. In contrast, the second deglacial pulse towards the end of the Younger Dryas is systematically present, independently from the fast atmospheric variability chosen. The magnitude of this second pulse is about 2 metres per century for all the different combinations and is closely tight to the PLISI. With these sensitivity experiments, we thus show that the evolution of the rate of ice loss for low value of the fast variability factor resembles the one of the coupled experiment. This is somewhat expected since the coupled model failed to capture the abrupt climatic transition during the deglaciation. Nonetheless, these experiments confirm the importance of the PLISI which systematically occurs regardless of the climatic scenario to drive the ice sheet model.

References

Abe-Ouchi, A., Saito, F., Kageyama, M., Braconnot, P., Harrison, S. P., Lambeck, K., ... Takahashi, K. (2015, November). Ice-sheet configuration in the CMIP5/PMIP3 Last Glacial Maximum experiments. *Geoscientific Model Development*, *8*(11), 3621–3637. doi: 10.5194/gmd-8-3621-2015

Beckmann, A., & Goosse, H. (2003). A parameterization of ice shelfocean interaction for climate models. *Ocean Modelling*, *5*(2), 157–170. doi: 10.1016/S1463-5003(02)00019-7

Benn, D. I., Warren, C. R., & Mottram, R. H. (2007, June). Calving processes and the dynamics of calving glaciers. *Earth-Science Reviews*, *82*(3), 143–179. doi: 10.1016/j.earscirev.2007.02.002

Berends, C. J., & Wal, R. S. W. v. d. (2016, December). A computationally efficient depression-filling algorithm for digital elevation models, applied to proglacial lake drainage. *Geoscientific Model Development*, *9*(12), 4451–4460. doi: 10.5194/gmd-9-4451-2016

Charbit, S., Ritz, C., Philippon, G., Peyaud, V., & Kageyama, M. (2007, January). Numerical reconstructions of the Northern Hemisphere ice sheets through the last glacial-interglacial cycle. *Climate of the Past*, *3*, 15–37.

Clarke, G. K. C., Leverington, D. W., Teller, J. T., & Dyke, A. S. (2004, February). Paleohydraulics of the last outburst flood from glacial Lake Agassiz and the 8200BP cold event. *Quaternary Science Reviews*, *23*(3), 389–407. doi: 10.1016/j.quascirev.2003.06.004

Dee, D. P., Uppala, S. M., Simmons, A. J., Berrisford, P., Poli, P., Kobayashi, S., ... Vitart, F. (2011, April). The ERA-Interim reanalysis: configuration and performance of the data assimilation system. *Quarterly Journal of the Royal Meteorological Society*, *137*(656), 553–597. doi: 10.1002/qj.828

Heinemann, M., Timmermann, A., Elison Timm, O., Saito, F., & Abe-Ouchi, A. (2014). Deglacial ice sheet meltdown: orbital pacemaking and CO2 effects. *Clim. Past*, *10*(4), 1567–1579. doi: 10.5194/cp-10-1567-2014

Ivanovic, R. F., Gregoire, L. J., Kageyama, M., Roche, D. M., Valdes, P. J., Burke, A., ... Tarasov, L. (2016). Transient climate simulations of the deglaciation 21–9 thousand years before present (version 1) PMIP4 Core experiment design and boundary conditions. *Geoscientific Model Development*, *9*(7), 2563–2587. doi: 10.5194/gmd-9-2563-2016

Peltier, W. R., Argus, D. F., & Drummond, R. (2015). Space geodesy constrains ice age terminal deglaciation: The global ICE-6G_c (VM5a) model. *Journal of Geophysical Research: Solid Earth*, *120*(1), 450–487. doi: 10.1002/2014JB011176

Quiquet, A., Dumas, C., Ritz, C., Peyaud, V., & Roche, D. M. (2018, dec). The GRISLI ice sheet model (version 2.0): calibration and validation for multi-millennial changes of the Antarctic ice sheet. *Geoscientific Model Development*, *11*(12), 5003–5025. doi: 10.5194/gmd-11-5003-2018

Quiquet, A., Roche, D. M., Dumas, C., & Paillard, D. (2018, feb). Online dynamical downscaling of temperature and precipitation within the *i*LOVECLIM model (version 1.1). *Geoscientific Model Development*, *11*(1), 453–466. doi: 10.5194/

gmd-11-453-2018

Roche, D. M., Dumas, C., Bügelmayer, M., Charbit, S., & Ritz, C. (2014, July). Adding a dynamical cryosphere to iLOVECLIM (version 1.0): coupling with the GRISLI ice-sheet model. *Geosci. Model Dev.*, *7*(4), 1377–1394. doi: 10.5194/gmd-7-1377-2014

Roche, D. M., Paillard, D., Caley, T., & Waelbroeck, C. (2014, December). LGM hosing approach to Heinrich Event 1: results and perspectives from datamodel integration using water isotopes. *Quaternary Science Reviews*, *106*, 247–261. doi: 10.1016/j.quascirev.2014.07.020

Stuhne, G. R., & Peltier, W. R. (2017). Assimilating the ICE-6G_c Reconstruction of the Latest Quaternary Ice Age Cycle Into Numerical Simulations of the Laurentide and Fennoscandian Ice Sheets. *Journal of Geophysical Research: Earth Surface*, *122*(12), 2324–2347. doi: 10.1002/2017JF004359

Tarasov, L., Dyke, A. S., Neal, R. M., & Peltier, W. R. (2012, January). A data-calibrated distribution of deglacial chronologies for the North American ice complex from glaciological modeling. *Earth and Planetary Science Letters*, *315-316*, 30–40. doi: 10.1016/j.epsl.2011.09.010

Trüssel, B. L., Motyka, R. J., Truffer, M., & Larsen, C. F. (2013). Rapid thinning of lake-calving Yakutat Glacier and the collapse of the Yakutat Icefield, southeast Alaska, USA. *Journal of Glaciology*, *59*(213), 149–161. doi: 10.3189/2013J0G12J081

Tsai, V. C., Stewart, A. L., & Thompson, A. F. (2015). Marine ice-sheet profiles and stability under Coulomb basal conditions. *Journal of Glaciology*, *61*(226), 205–215. doi: 10.3189/2015JoG14J221 van den Berg, J., van de Wal, R., & Oerlemans, H. (2008, April). A mass balance model for the Eurasian Ice Sheet for the last 120,000years. *Global and Planetary Change*, *61*(3), 194–208. doi: 10.1016/j.gloplacha.2007.08.015

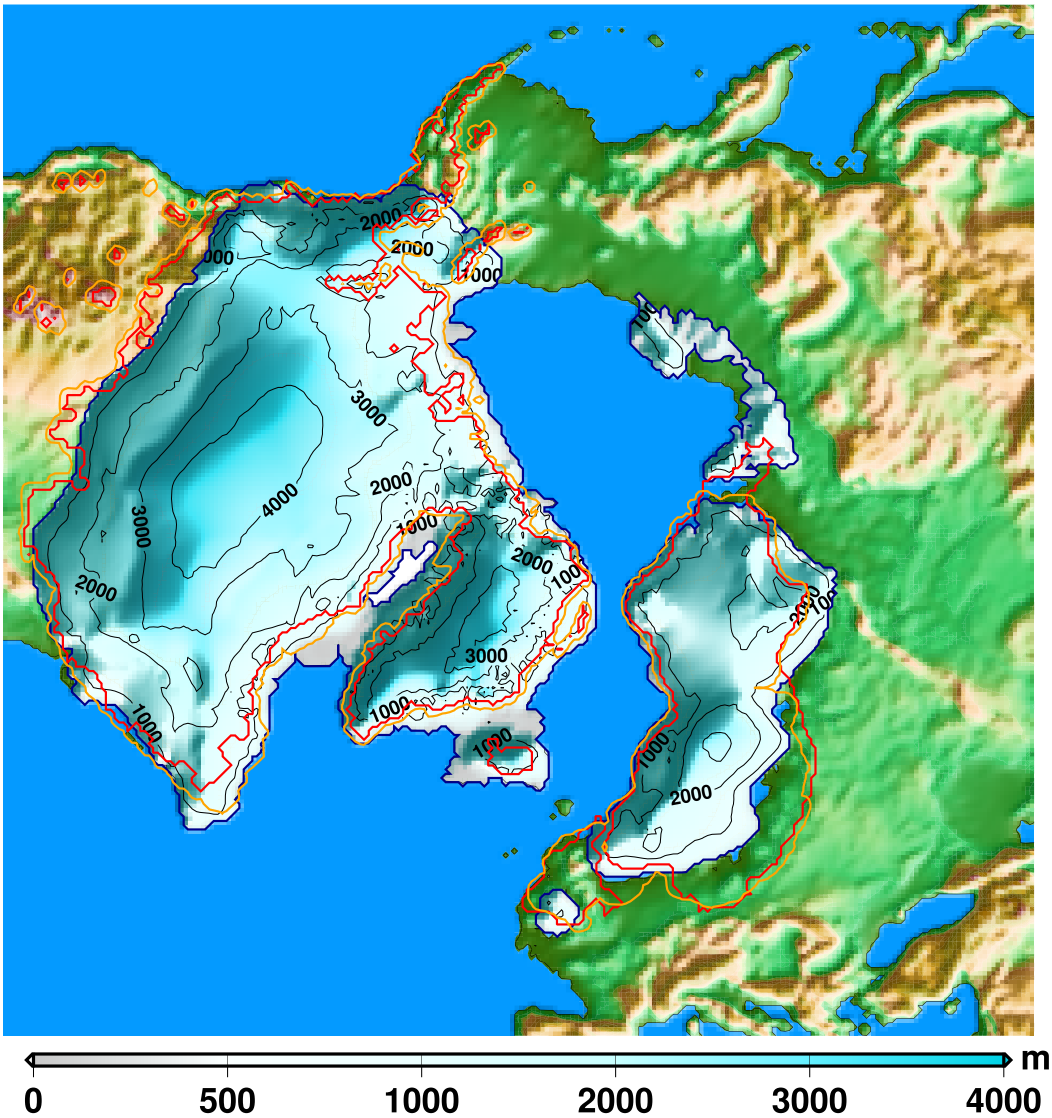

Figure S1. Simulated Northern Hemisphere ice sheets with iLOVECLIM-GRISLI at the last glacial maximum (21 kaBP). Isocontours for ice thickness are represented every 1000 metres and the grounding line is the dark blue line. The extent of ICE-6G_C and GLAC-1D are depicted in red and orange, respectively.

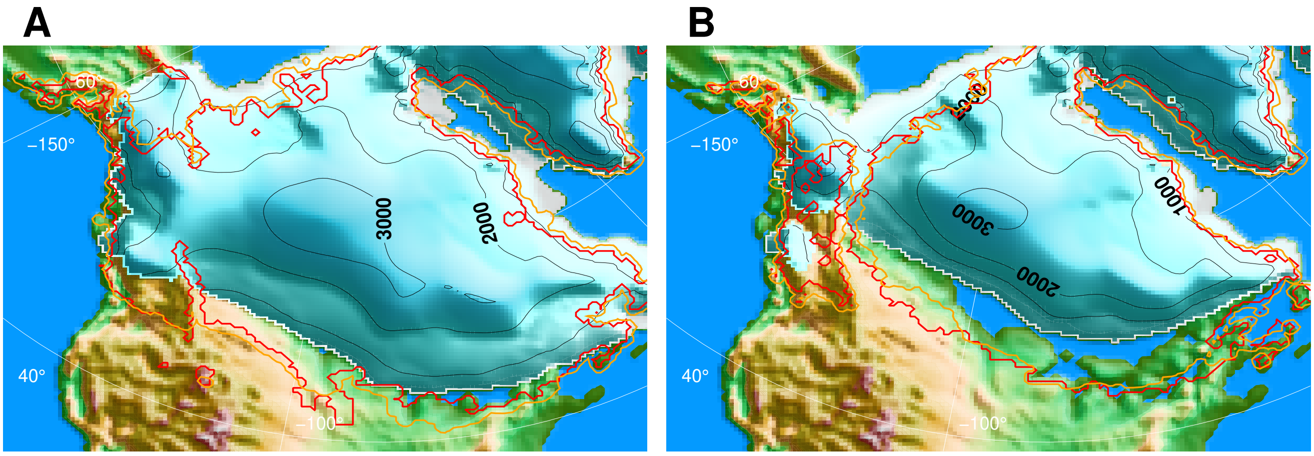

Figure S2. Simulated NAIS at the early stages of the deglaciation. Simulated NAIS with iLOVECLIM-GRISLI at 16 kaBP (A) and at 14 kaBP (B). Isocontours for ice thickness are represented every 1000 metres. The extent of ICE-6G_C and GLAC-1D are depicted in red and orange, respectively.

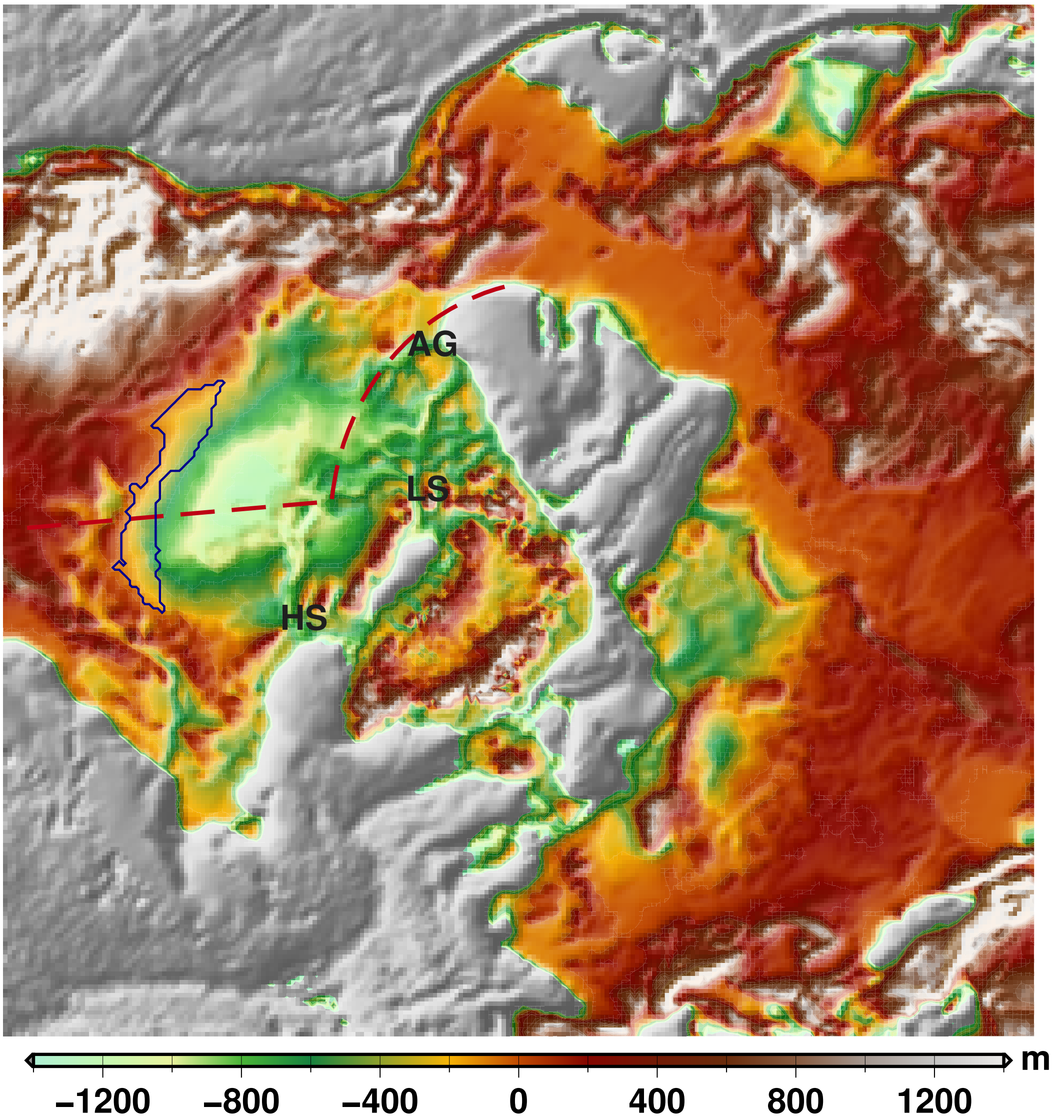

Figure S3. Simulated bedrock topography with iLOVECLIM-GRISLI at 13.8 kaBP. Elevation given in metres above present-day sea level. The simulated extent of proglacial lake Agassiz-Ojibway is contoured dark blue line. The dashed red line represents the ice sheet cross-section presented in the manuscript. The ice streams discussed in the text are: Amundsen Gulf (AG), Lancaster Sound (LS) and Hudson Strait (HS).

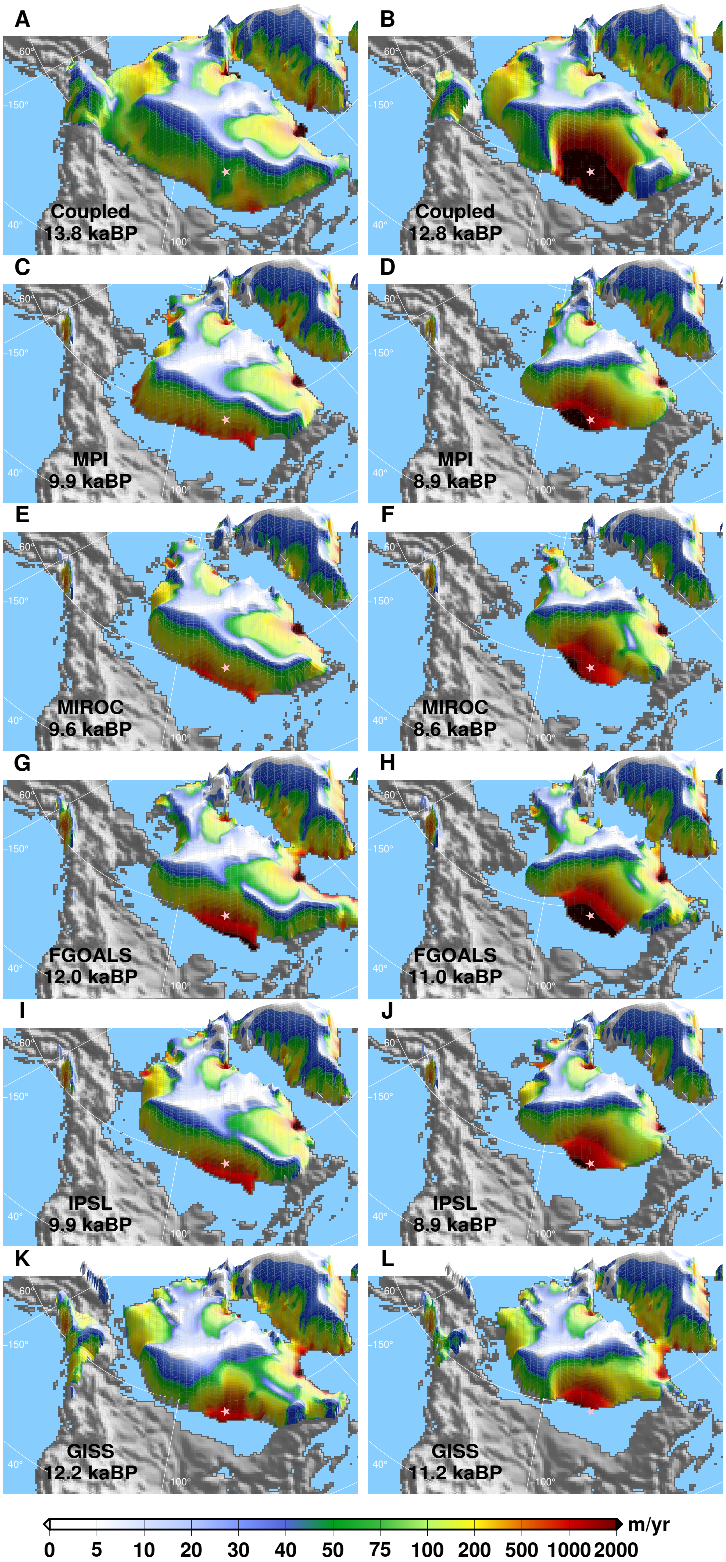

Figure S4. Ice sheet geometries at the time of the instability. Vertically integrated velocity before (left) and after (right) the maximum in rate of NAIS ice loss. Each row corresponds to a specific climate scenario: the coupled experiment (A,B) and the five stand-alone experiments using MPI-ESM-P (C,D), MIROC-ESM (E,F), FGOALS-g2 (G,H), IPSL-CM5A-LR (I,J) and GISS-E2-R (K,L). The stand-alone experiments shown here use a weighing factor for the fast variability of 0.25. For a given climate scenario, the two snapshots presented here are separated by one thousand year with the left-hand side at 13.8 kaBP (A), 9.9 kaBP (C), 9.6 kaBP (E), 12.0 kaBP (G), 9.9 kaBP (I) and 12.2 kaBP (K). For this 3-D perspective plot, the velocity is draped on top of the ice sheet topography. The pink star is the selected grid point for the time evolution of the ice flux shown in Fig. S8.

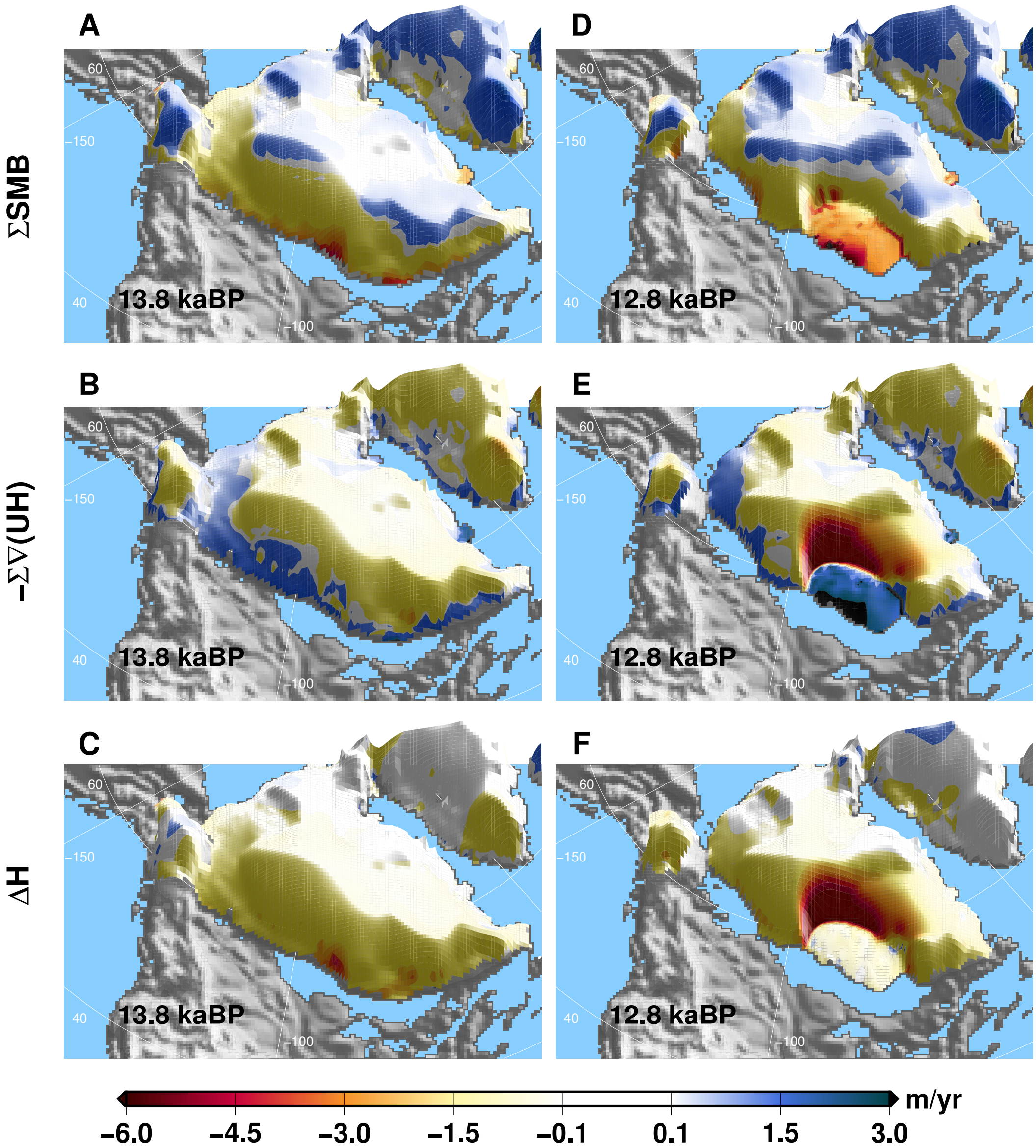

Figure S5. Respective role of surface mass balance with respect to ice dynamics. Total ice thickness change (expressed in metre per year) breakdown (Eq. 3) in the coupled experiment over a 100 year window: integrated surface mass balance (A,D), integral of the opposite of the ice flux divergence (B,E) and resulting change in ice thickness (C,F). The computations are done before (A,B,C, 13.8 kaBP – 13.7 kaBP) and after (D,E,F, 12.8 kaBP – 12.7 kaBP) the PLISI event.

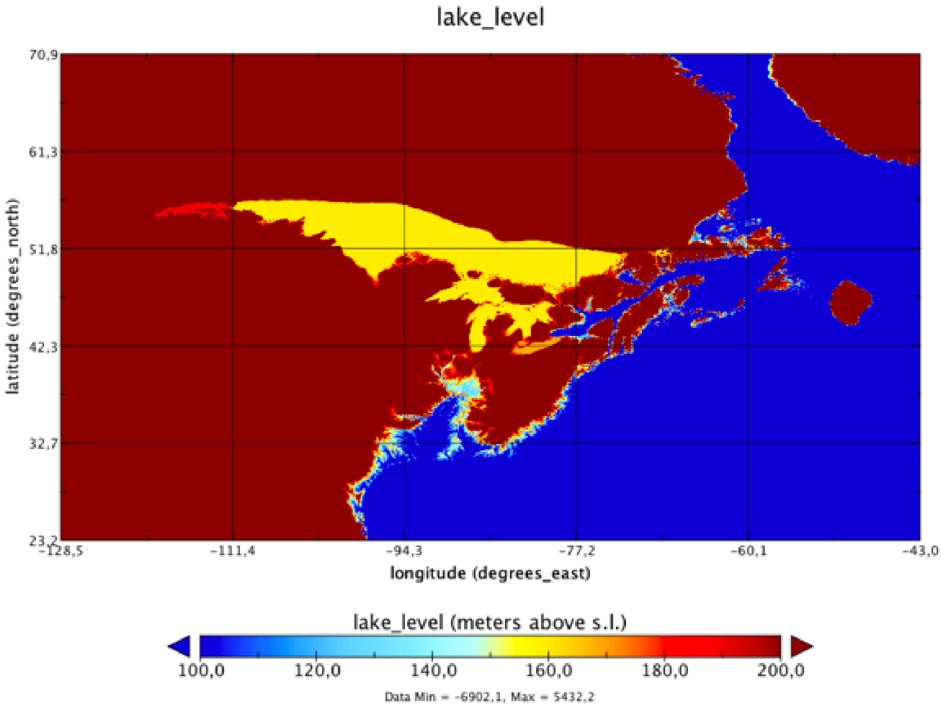

Figure S6. Example of a lake level computed using a 14 kaBP simulated ice sheet topography. The yellow area stands for a lake level at about 160 m above present-day sea level, so about 235 m above the 14 kaBP sea level.

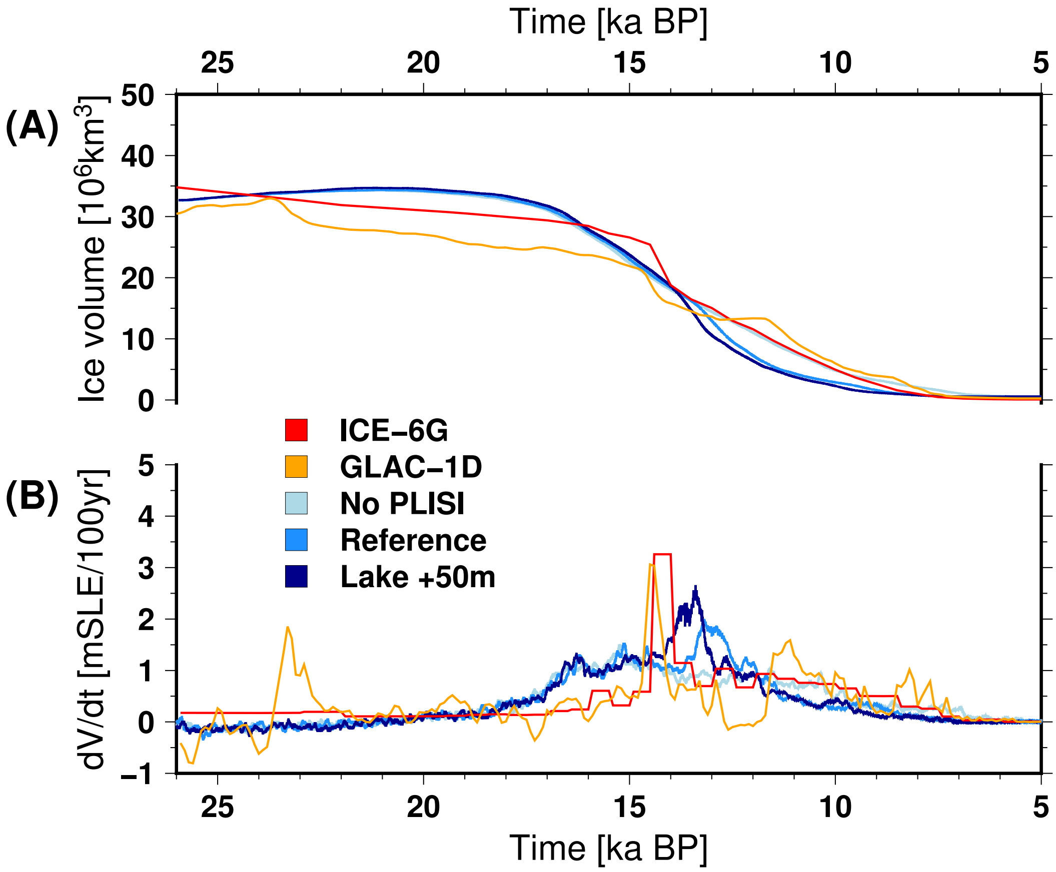

Figure S7. Importance of the PLISI for the temporal evolution. Simulated total ice volume (A) and rate of ice loss (expressed as ice volume contributing to sea level rise per century) (B) through the deglaciation (26 kaBP – 5 kaBP) for the NAIS using the GRISLI-iLOVECLIM set-up when we prevent the PLISI occurrence (light blue), in the standard configuration (lake level follows the eustatic sea level forcing, blue) and with a lake level at +50 metres above present-day at all times (dark blue). The ice sheet volume and rate of volume change of GLAC-1D and ICE-6G are shown in orange and red, respectively.

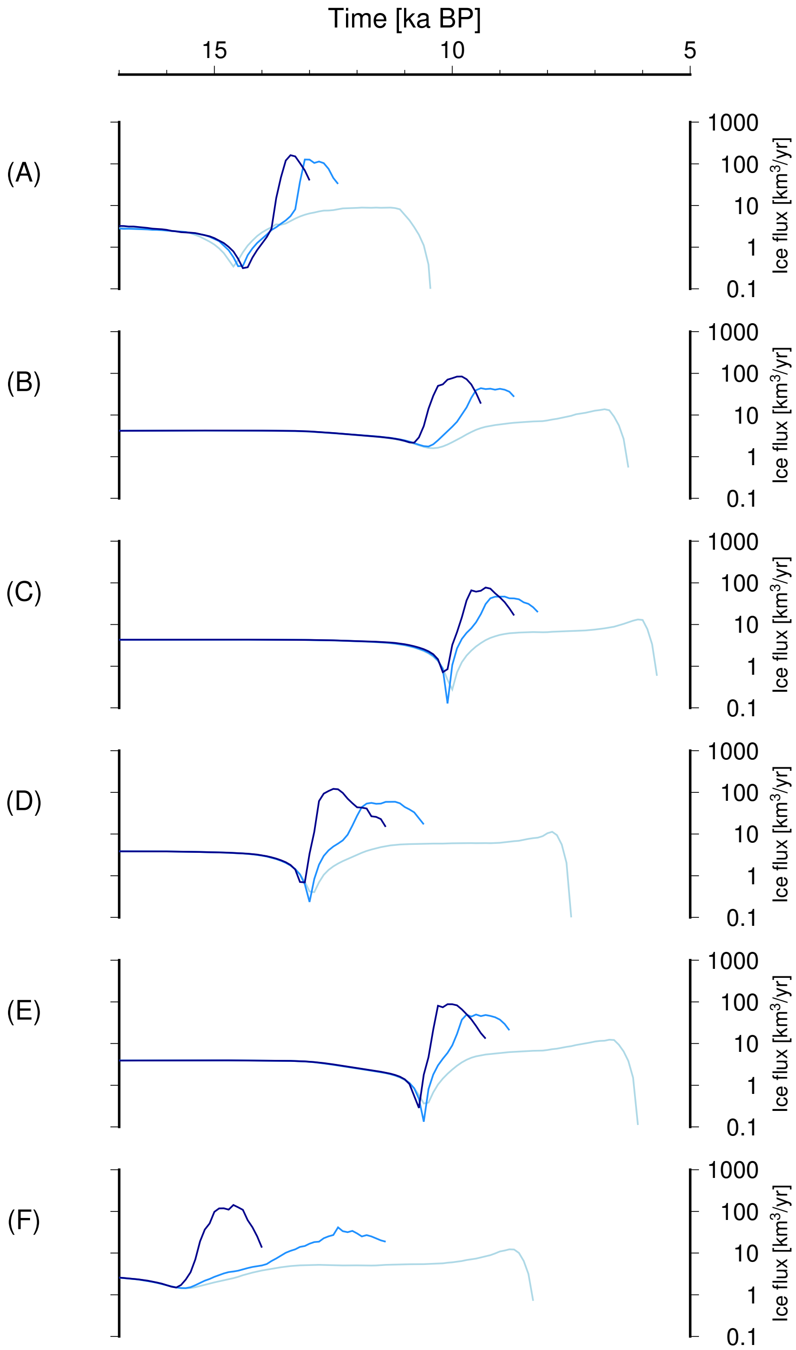

Figure S8. Importance of the PLISI for the ice flux. Simulated ice flux for a selected point affected by the PLISI (86.1 °W, 58.3 °N shown in Fig. S4) when we prevent the PLISI occurrence (light blue), in the standard configuration (lake level follows the eustatic sea level forcing, blue) and with a lake level at +50 metres above present-day at all times (dark blue) for the coupled experiment (A) and for a set of stand-alone ice sheet experiments forced by PMIP4 outputs: MPI-ESM-P (B), MIROC-ESM (C), FGOALS-g2 (D), IPSL-CM5A-LR (E) and GISS-E2-R (F). The stand-alone experiments here use a weighing factor for the fast variability of 0.25. The vertical scale is logarithmic. The curves stop when local ice thickness reaches zero.

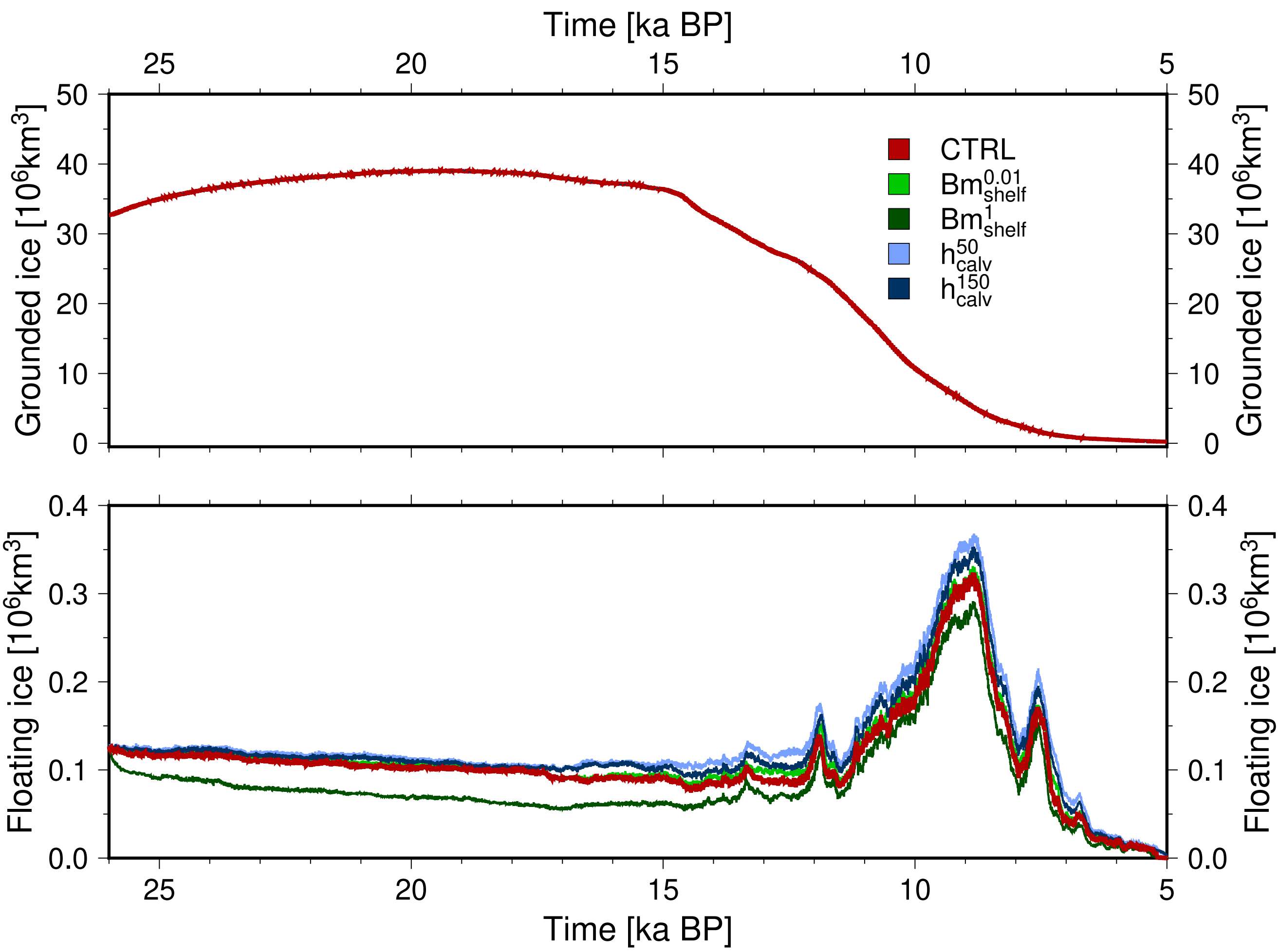

Figure S9. Importance of sub-shelf melt and calving rates. NAIS grounded ice volume (top) and volume of ice above flotation (bottom) for a set of sensitivity experiment. CTRL experiments for this figure is a stand-alone ice sheet simulation using the MPI-ESM-P climate anomalies with a weighing factor for the fast variabil ity of 0.25. The green curves represent experiments that use the same setup as the CTRL except that they have a constant sub-shelf melt rates of 0.01 m yr^{-1} (light green) and 1 m yr^{-1} (dark green) instead of using a time-varying sub-shelf melt rate (near 0 at the LGM and 0.3 for the pre-industrial). The blue curves also represent experiments that use the same setup as the CTRL except that they have an ice thickness threshold for calving of 50 m (light blue) and 150 m (dark blue) instead of 250 m in the CTRL.

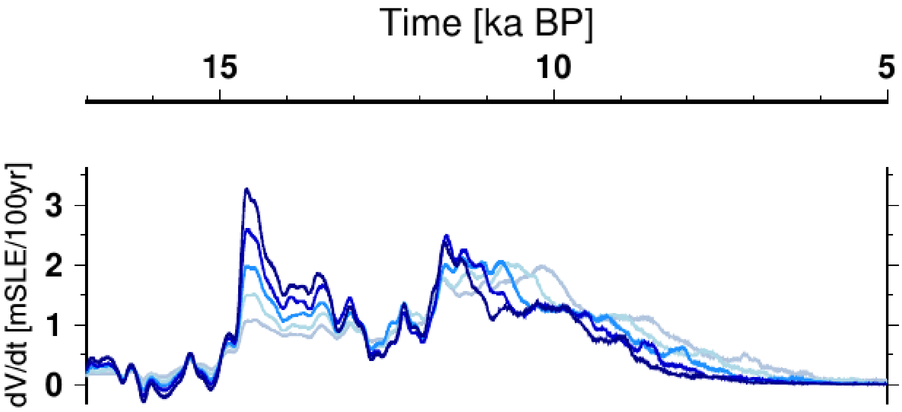

Figure S10. Importance of the fast variability weighing factor for stand-alone ice sheet simulations. Rate of NAIS ice loss through the deglaciation (17 kaBP – 5 kaBP) for stand-alone ice sheet simulations using MPI-ESM-P. The different curves are obtained with different value for the atmospheric fast variability weighing factor r (see Methods). The color gradients represent the importance given to the fast variability, from little importance (light grey, $r = 0.15$) to great importance (dark blue, $r = 0.55$).

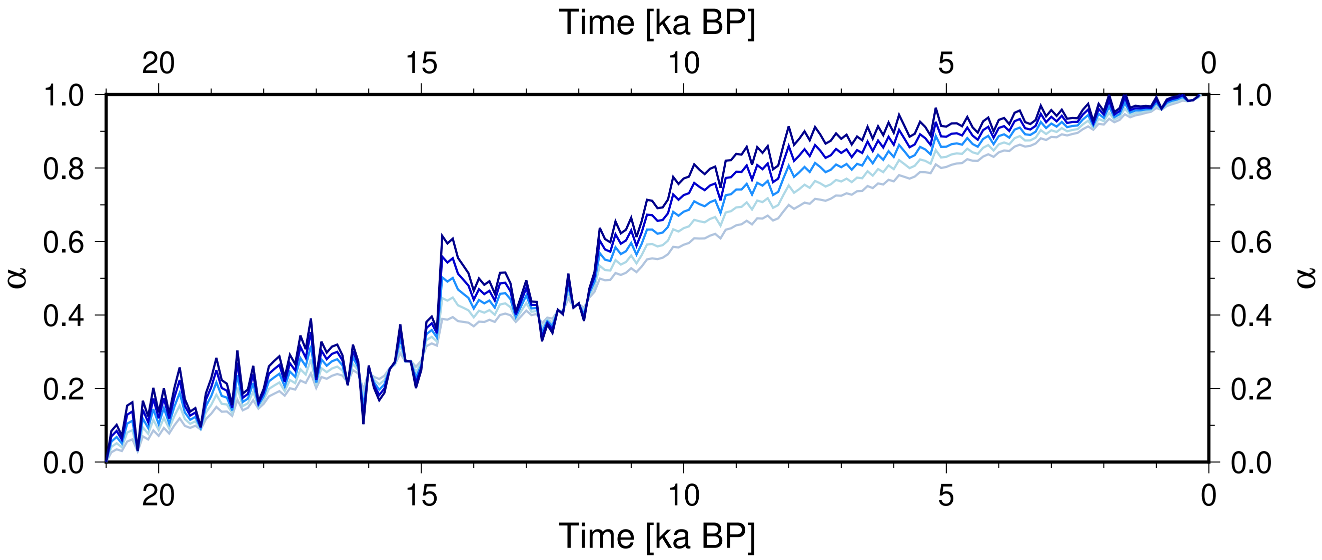

Figure S11. Glacial index used for the stand-alone experiments for a range of fast variability weighing factor r. The color gradients represent the importance given to the fast variability, from little importance (light grey, $r = 0.15$) to great importance (dark blue, $r = 0.55$).